

Multi-wavelength diagnostic properties of Galactic Planetary Nebulae detected by GLIMPSE-I

Martin Cohen¹, Quentin A. Parker^{2,3}, Anne J. Green⁴, Brent Miszalski^{2,5}, David Frew²,
Tara Murphy^{4,6}

¹*Radio Astronomy Laboratory, University of California, Berkeley, CA 94720, USA*

²*Department of Physics, Macquarie University, Sydney, NSW 2109 Australia*

³*Anglo-Australian Observatory, PO Box 296, Epping, NSW 2121, Australia*

⁴*Sydney Institute for Astronomy, School of Physics, The University of Sydney, NSW 2006, Australia*

⁵*Centre for Astrophysics Research, STRI, University of Hertfordshire, College Lane Campus, Hatfield AL10 9AB, UK*

⁶*School of Information Technologies, The University of Sydney, NSW 2006, Australia*

Accepted . Received ; in original form

ABSTRACT

We uniformly analyze 136 optically detected PNe and candidates from the GLIMPSE-I survey in order to develop robust, multi-wavelength, classification criteria to augment existing diagnostics and provide pure PN samples. PNe represent powerful astrophysical probes. They are important dynamical tracers, key sources of ISM chemical enrichment, windows into late stellar evolution, and potent cosmological yardsticks. But their utility depends on separating them unequivocally from the many nebular mimics which can strongly resemble *bona fide* PNe in traditional optical images and spectra. We merge new PNe from the carefully evaluated, homogeneous MASH-I and MASH-II surveys, which offer a wider evolutionary range of PNe than hitherto available, with previously known PNe classified by SIMBAD. Mid-infrared (MIR) measurements vitally complement optical data because they reveal other physical processes and morphologies via fine-structure lines, molecular bands and dust. MIR colour-colour planes, optical emission line ratios and radio fluxes show the unambiguous classification of PNe to be complex, requiring all available evidence. Statistical trends provide predictive value and we offer quantitative MIR criteria to determine whether an emission nebula is most likely to be a PN or one of the frequent contaminants such as compact HII regions or symbiotic systems. Prerequisites have been optical images and spectra but MIR morphology, colours, environment and a candidate's MIR/radio flux ratio provide a more rigorous classification. Our ultimate goal is to recognize PNe using only MIR and radio characteristics, enabling us to trawl for PNe effectively even in heavily obscured regions of the Galaxy.

1 INTRODUCTION

Planetary nebulae (PNe) are the resolved, ionized gas shrouds of dying stars. PNe are expected to be numerous as their progenitors are the evolved cores of stars once in the mass range 1-8 times that of the sun that represent 90 percent of all stars more massive than the sun. Estimates suggest that there may be as few as 5,000 (Moe & De Marco 2006a) but as many as 24,000 PNe (Frew, 2008) in our Galaxy although fewer than 3000 are currently known (Frew & Parker 2010). The role of PNe in our Galaxy is significant since its chemical evolution depends critically on the amount of enriched mass recycled by PN progenitor stars via all mass loss episodes including the final PN ejection. These ejecta are significantly enriched by stellar nuclear processes. In the first giga-year of galaxy evolution supernova explosions and high-mass PN progenitors return about the same gross mass but thereafter the PN contribution increasingly dominates. Low and intermediate mass stars are an additional source of pre-biotic carbon later in the interstellar medium (ISM), returned in their PN phase, although massive stars return more (Gustafsson et al. (1999, Henry, Edmunds & Köppen 2000). However, the thin disc and metal-rich thick disc of our Galaxy gain most carbon from low- and intermediate-mass stars (Bensby & Feltzing 2006) as do any regions with higher metallicity (Chiappini et al. 2003).

PNe exhibit strong emission lines making them detectable to great distances and this allows determination of accurate velocities and expansion rates (from which PN dynamical ages can be gauged) across the entire Galaxy. Importantly, the luminosity distribution of PNe in external galaxies allows their use as distance calibrators in determining the scale of the Universe to an accuracy of about 10 percent (e.g. Jacoby 1989, Ciardullo et al. 2002, 2006; Ciardullo 2010). This luminosity distribution encodes rich information on our Galaxy's star-forming history. More parochially, the complex morphologies of PNe provide clues to their formation, evolution, mass loss processes, and the shaping role played by binary central stars or even sub-stellar objects and planets (Soker (2004), Miszalski et al. 2009a). Also, as the central star rapidly fades to become a white dwarf and the nebula expands, the integrated flux, surface brightness and radius all change in a way that can be predicted by current stellar and hydrodynamic theory.

In all these ways, PNe are effective astrophysical probes which have particular utility if their distances are also known (currently a major problem in the field). We have made recent progress here with the adoption of a new surface-brightness radius relation that shows great promise (e.g Frew 2008, Frew & Parker 2010), as we demonstrate later.

However, a major problem that has undermined the value of previous PNe catalogues is the presence of contaminants. Precise PN identification is complicated by the wide variety of morphologies, ionization characteristics and surface brightness distributions of the PN family which reflects the stages of nebular evolution, progenitor mass and chemistry and the possible influence of common envelope binaries (e.g. De Marco 2009, Miszalski et al. 2008a, 2009a). Frew (2008) for example, has recently shown that up to 15 percent of objects currently accepted as nearby PNe (e.g. Hewett et al. 2003) are actually just ionized regions of the general ISM around hot white dwarf or subdwarf stars (e.g. Frew & Parker 2006, Frew & Parker 2010).

Our group has now tested and adopted a range of criteria to eliminate such contaminants more effectively. Only the recent on-line availability of imaging surveys and other data has enabled such clear discrimination tools to be developed (e.g. Parker et al. 2006;

Madsen et al. (2006), Frew & Parker 2010). In this paper we particularly emphasize the power of the newly available high quality, high-resolution and deep MIR imaging in the Spitzer GLIMPSE survey to contribute to robust PN identification.

The field of MIR work on PNe is highly active now, with contributions from Chu et al.(2009); Hora et al. (2004), Kwok et al. (2008); Madsen et al. (2006), Phillips & Ramos-Larios 2008,2009), Phillips & Zepeda-Garcia (2009), and Ramos-Larios & Phillips (2008). Cohen et al. (2007a: hereafter Paper-I) undertook a preliminary initial analysis of MASH-I PNe (Macquarie-AAO-Strasbourg H α PN Project: Parker et al. 2006), observed by the Spitzer GLIMPSE project. Optical, MIR, and radio characteristics were examined and combined. Although the results were limited to a sample of only 54 PNe, Paper-I had examples of objects rejected as non-PNe and adduced reasons for their rejections. It probed the detailed spatial relationships between H α and MIR images, and it established an ensemble value for the MIR/radio flux ratio in PNe that was almost the same as we derive here. The current paper follows on from Paper-I. In the intervening period, the MASH-II catalogue has been created by Miszalski et al. (2008b). Unlike MASH-I PNe, which were discovered on the AAO/UKST/ H α survey by visual methods, the many compact MASH-II nebulae were found by semi-automated techniques applied to the image parameterization data from the digitized version of the original photographic film material, e.g. Hambly et al. (2001). Seventy-five percent of new MASH-II PNe were found using the Image Analysis Mode of the SuperCosmos data pipeline (Hambly et al. (2001) to target star-like or compact PNe. The remaining 25 percent are highly evolved, very low surface brightness, extended PNe, uncovered only by quotient imaging of the factor 16 blocked down matching H α and R-band exposures. A fully detailed description of MASH-II discovery techniques is given by Miszalski et al. (2008b). The verification of nebulae as *bona fide* PNe is primarily achieved by follow-up ground-based optical spectroscopy, exactly as for MASH-I. Hundreds of MASH-II PNe candidates were discovered and currently 360 are classified as true (T), likely (L) or possible (P) PNe following a similar procedure to that for MASH-I. The combined MASH-I and MASH-II catalogues cover the same region of the Galaxy and together effectively span the full evolutionary range of PNe from the young, high density compact PNe to those dissipating into the ambient ISM. Although MASH-I and MASH-II probe the same Galactic volume and include the same types of nebulae, the respective fractions of compact PNe and extremely evolved PNe are different. An objective of the current paper is to compare the multi-wavelength attributes of the two sets of MASH PNe and previously known PNe. We also emphasize the vital importance of a rigorous uncontaminated sample of PNe. This is done by utilizing the discriminatory power inherent in homogeneous multi-wavelength surveys, and by developing associated diagnostic criteria with strong predictive capability. Some cautionary notes on traps that occur in applying sweeping generalizations with limited data are also made.

In §2 we describe our selection of nebulae and discuss techniques to remove non-PNe from existing PNe catalogues. §3 presents our sample of PNe which we believe constitutes a “clean” sample of 136 nebulae to satisfy our stringent selection criteria. §4 discusses the spatial distributions of MIR emission in nebulae of large apparent diameter. §5 addresses the classification of nebular morphologies. §6 offers a series of analyses of PNe based on measured IRAC MIR colours, optical emission-line flux ratios, IRAC false colours, radio continuum fluxes and MIR/radio ratios. In §6 we also compare the IRAC colours of PNe, drawn from several subgroups, with the colours of diffuse and compact and ultra-compact

HII regions (UCHIIs) and we explore IRAC colour-colour planes and determine which combination of colours might best separate PNe from contamination by other kinds of source. Another objective is to seek the largest metric distances in the colour-colour planes between the locations of PNe and of their contaminants, and we demonstrate statistically significant quantitative discriminants between PNe and objects frequently confused with PNe. §7 investigates whether the diagnostic diagram of common emission line ratios first proposed by Sabbadin, Minelo, & Biancini (1977: SMB) has any utility for this set of PNe when separating them by their discovery method, optical spectral lines, their MIR false colours, age, or their morphology. §8 examines the properties of our PNe in relation to their derived ages. §9 examines the radio properties and the median MIR/radio flux ratios for different subsets of PNe and in relation to age. §10 seeks the possibility of a link between MIR false colours and nebular excitation, PN type and MIR/radio ratio. §11 compares the colours of Galactic and LMC PNe. §12 presents our conclusions.

The appendix summarizes those objects which we, and others, have rejected as PNe, in the hope that this list will help PN investigators to drop these contaminants from their own studies of PNe. These objects should be withdrawn from the PN literature, principally from SIMBAD, although some of this updating has already occurred with the incorporation of MASH nebulae into Vizier.

2 SAMPLE SELECTION

The defining criteria of our sample are i) that all objects have been assigned to the category of PNe either in the new MASH-I or MASH-II databases (available through Vizier) or via current listing in SIMBAD as a PN and ii) must lie within the area covered by GLIMPSE-I (Benjamin et al. 2003; Churchwell et al. 2009), and iii) within the Galactic longitude boundaries of the SuperCosmos H α Survey of the Southern Galactic plane (SHS: Parker et al. 2005). The SHS was the discovery medium for MASH and, therefore, all these PNe have optical counterparts. This is unlike the possible PN identified at (313.355, +0.312), reported by Cohen et al. (2005) based solely on radio and MIR data since no meaningful optical emission could be established due to excessive extinction along the PN sight line.¹ Finally, together with the GLIMPSE longitude limits of 10° to 65°, and 295° to 350°, we also chose to cut at Galactic latitudes of $\pm 1.16^\circ$. The boundaries of the GLIMPSE area are jagged beyond $\pm 1.0^\circ$ in latitude because the individual Spitzer IRAC frames were not laid down in the sky parallel to Galactic coordinate axes. Twenty-one PNe close to the latitude limits of GLIMPSE had incomplete wavelength coverage (3.6 and 5.8 μm , or 4.5 and 8.0 μm). In Paper-I the latitude range of the PN sample was $\pm 1.0^\circ$. Consequently our sample of MASH-I PNe with the new, broader limits was enlarged to 66 objects; 12 more than for Paper-I. It also includes 31 new MASH-II nebulae. Note that a number of PNe initially discovered by MASH have subsequently entered the literature under other designations while MASH databases were being finalized.

Our third sample consists of 44 PNe recorded in the literature

prior to the MASH surveys. This sample represents the heterogeneous “known” PNe compiled historically from disparate sources into, for example, the Acker (1992, 1996) and Kohoutek (2001) PN catalogues. These were added as these previously known putative PNe may not be representative of the full PN evolutionary range compared to MASH nebulae and also because they have not been filtered through the same diagnostic criteria used to identify PNe in MASH and, therefore, may contain higher levels of contaminants. After Acker’s catalogues and during the observing period of MASH, many papers appeared containing small numbers of new PNe and some of these non-MASH PNe look very much like those preferentially discovered by MASH; for example, the objects found by Beer & Vaughan (1999), Cappellaro et al. (2001), and Boumis et al. (2003, 2006).

2.1 Removing contaminants from PN catalogues

2.1.1 Identifying MASH contaminants

Although careful assessment of candidate PNe was made in compiling MASH catalogues in the first place (Parker et al. 2006, Miszalski et al. 2008b) they have been critically re-examined here based on a combined multi-wavelength approach incorporating GLIMPSE data, rather than via assessment of merely optical and NIR/MSX attributes (e.g. Cohen et al. 2007a). Indeed, as higher quality, deeper, optical spectra are acquired by the MASH consortium for poorly studied MASH PNe, lines too weak to have been recognized in the original confirmatory spectra of the nebulae can call into doubt the original PN classification, especially for compact or barely resolved objects. As a result several MASH objects have been re-classified as symbiotic stars, e.g. PHR1253-6350 (Paper-I).

One technique used for original MASH culling was based on 2MASS colour-colour plots, e.g. Schmeja & Kimeswenger (2001), Corradi et al. (2008). Coding 2MASS J, H, K_s images as blue, green and red, respectively, then combining them into a false-colour composite can also be a valuable discriminator. True unresolved PNe appear violet in 2MASS false colours while resolved PNe are often purple in 2MASS. In general this is due to the inclusion of the strongest emission lines in the J-band (1.25 μm) and K_s band (2.16 μm). The relevant expected PN lines were listed by Whitelock (1985) who forecast the great strength of the HeI triplet at 1.083 μm . This prediction has been well demonstrated (e.g. for NGC 7027, by Treffers et al. 1976). The IR spectral line content of PNe was revisited by Hora et al. (1999) on the basis of 1–2.5- μm spectroscopy. These authors divided their PN sample into groups, according to the dominance of the continuum or emission lines of H α and/or H $_2$.

These characteristics determine the strongest emission lines in the JHK bands. For example, in H α line-dominated PNe, for J , Paschen β is the brightest line, augmented by 1.083- μm HeI, 1.26- μm [FeII], and 1.316- μm OI; for H , the H α Brackett series dominates, with contributions from 1.700- μm H α and 1.644- μm [FeII] (the latter in PNe with internal shocks); for K , Br γ , HeI at 2.058 and 2.112- μm , with bright 2.122- μm of H $_2$ present in some PNe (see §4).

Another major source of PN contaminants are diffuse, compact, and UCHIs. If high signal-to-noise optical spectra are lacking it may prove impossible to discriminate between some very low excitation PNe and some HII regions because the relative strengths of the [OIII], H β , H α , and [NII] lines exhibited by both types of nebula can overlap (e.g. see Frew & Parker 2010). Our multi-spectral approach to nebular discrimination and the various spectral

¹ We have recently noted possible very faint H α emission in a quotient image of the vicinity of the IR ring. This is too weak to define any morphology and no optical spectrum is yet available.

and photometric signatures for most PNe contaminants has recently been reviewed by Frew & Parker (2010).

In this paper we specifically reveal how the MIR morphology of nebulae can provide a valuable additional discrimination tool because true UCHIIs are only rarely unresolved by IRAC at $8\,\mu\text{m}$ (Cohen et al. 2007b).

2.1.2 The discriminatory power of MIR and radio data

The presence of filaments, extended structures and/or an amorphous halo in the MIR imagery, exterior to the optical image, generally indicates an HII region rather than a PN. We draw a clear distinction between the generally symmetrical, roundish photodissociation regions (PDRs) of PNe and the irregular streamers that Cohen et al. (2007b) identified. An excellent example of such a streamer is given by these authors in their Fig.18. False color also plays a role. PNe are found only in three false colours, none of them matched by the false colour of any HII region in the MIR.

Compact PNe which are isolated in the MIR are easy to identify but not every MIR-detected PN is compact nor isolated from other more extended MIR emission. Creating MIR false-colours images by representing the three IRAC bands at 4.5, 5.8, and $8.0\,\mu\text{m}$ by blue, green, red, respectively (hereafter IRAC false colour or MIR false colour) is also a valuable discriminatory tool (Paper-I) to identify PNe in more complex regions. For example, in their blind 20-GHz radio survey of the Galactic plane for UCHIIs, Murphy et al. (2010) noted that about 10 percent of their sample were easily recognized as PNe on the basis of their IRAC false colours which appear red, as opposed to the yellow (PAH emission) or white (broadband thermal emission by dust) of HII regions. This discrimination is further assisted via other indicators such as the lack of obvious association of true PNe with amorphous extended MIR structure and their low observed ratios of MIR to radio continuum (e.g. typically a value of ~ 5 compared with the median ratio of 42 for UCHIIs). The formal difference between these two independent medians is significant at the 5σ level (where σ combines the errors of these median ratios in quadrature). For PNe with well-known distances (e.g. such as those in the Magellanic Clouds), a large radio flux density ($\geq 5\text{ mJy}$) is found to be a promising discriminant between HII regions and PNe which typically are weak radio emitters (e.g. Filipovic et al. 2009). In short, there is an increasing number of criteria that can be used to characterize a nebula as a PN or contaminant in addition to the classical reliance on its optical morphology and spectrum. In their recent discussion of the changing landscape of PN classification Frew & Parker (2010) emphasize a problem with investigating extragalactic PN candidates, namely that high-resolution optical imagery is often lacking, rendering MIR and radio criteria even more important as parallel indicators.

Young stellar objects (YSOs) have also been cited as confused with known PNe (Whitney et al. 2008) in an LMC colour-magnitude diagram. The grid of precomputed energy distributions of YSOs (Robitaille et al. 2006) contains 200,000 spectra, and spans too vast an area to represent even by median colours. However, in order for a YSO spectrum to mimic that of a PN requires a large extinction, too large for any object discovered optically, and much more plausible for a YSO embedded in a dark cloud. Visual examination of the environs is usually adequate to distinguish a potential YSO from a PN.

Honing this new set of multi-wavelength discrimination tools so that one gains experience of the relative weighting of these di-



Figure 1. IRAC False colour image of Hen2-77 reveals the MIR morphology to be that of an UCHII with surrounding filamentary structure, and not a PN. Image is $4' \times 4'$. Galactic N and E are up and left.

verse criteria is an implicit goal of the present paper. We will emphasize the potential role of MIR properties of nebulae and their locations in colour-colour diagrams as further means both to eliminate contaminants from PN surveys and to refine traits and evolutionary characteristics of *bona fide* PNe.

2.2 Examples of ambiguous objects culled from the sample

There are many nebulous objects in the extant PN catalogues which have been notoriously difficult to classify by any number of previous litmus tests because the existing observational evidence is inconclusive or even contradictory. They often have conflicting identifications in SIMBAD. We select two such objects here to illustrate the additional discriminatory capabilities of the GLIMPSE MIR data that can finally shed light on the true nature of such objects.

2.2.1 Hen2-77

The first such object is Hen2-77 which has a long history of controversy in the literature. Roughly half the 75 articles in SIMBAD in which it is mentioned regard it as a PN. However, Cohen & Barlow (1980) concluded that it is a heavily reddened HII region because of its patchy, irregular optical appearance, lack of an identified central star, large radio continuum flux density, and its high A_V of 9, derived from the Balmer decrement. IRAC false colour imagery (Fig. 1) further reinforces the argument in favour of an HII region nature due to the character of its MIR morphology (Cohen et al. 2007b). Its 2MASS false colour counterpart (Fig. 2) shows an orange and white diffusely extended source rather than the normal purple colour of many PNe caused by the combination of strong [FeII] in the J-band and the S1 1-0 H_2 line in the K_s band.

Hen2-77 is indistinguishable from the many other sources in the surveys of HII regions by Caswell & Haynes (1987) and by Kuchar & Clark (1997), and other references to it as a thermal radio source can be found by examining the remainder of the 75 citations in the literature that do not conclude that it is a PN, particularly the more recent references since 2000, where its MIR spectral character is discussed. For example, Peeters et al. (2002) include it under

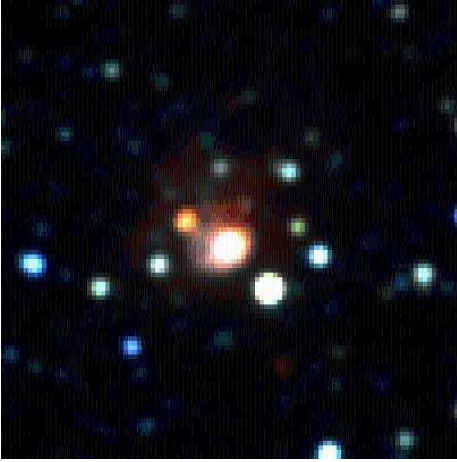


Figure 2. 2MASS false colour image of Hen2-77. Image is $100'' \times 100''$. Galactic N and E are up and left.

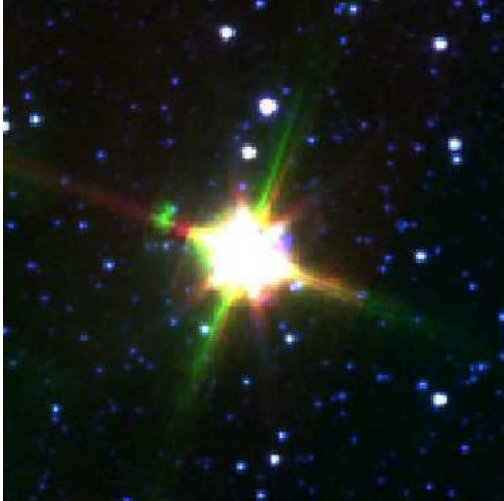


Figure 3. Mz 3 in IRAC false colour. The Spitzer diffraction spikes indicate the presence of a very compact, but unsaturated, central core. Image is $4' \times 4'$. Galactic N and E are up and left.

its IRAS name, IRAS 1206–6259, (it is also known as RAFGL 4144) in their MIR spectral catalogue of 45 compact HII regions. These authors derived a luminosity of $4.5 \times 10^5 L_{\odot}$, clearly marking it as an HII region.

There appear to be two separate nebulosities in the optical yet only a single MIR extended object that embraces both these nebulae. A dust lane might account for this. The dominant MIR core lies to the south-west and it contains a number of seemingly embedded point sources, perhaps a nascent cluster of stars. Unlike many PNe, the four IRAC images of Hen2-77 (Fig. 4) have the same size and structure. The IRAC false colour image (Fig. 1) shows a central white rhomboid, implying emission in all three bands and indicative of continuum thermal emission by dust grains. The core is enveloped by several faint, yellowish (probably PAH-emitting) filaments, very similar to other compact HII regions (Cohen et al. 2007b) and UCHIs (Murphy et al. 2010) but atypical of PNe. The yellow-green colour suggests PAH emission in the IRAC 5.8 and $8.0\text{-}\mu\text{m}$ bands, consistent with its MIR spectrum (e.g. Cohen et al. 1989), but clearly different from the orange and/or red false colours of PNe that are attributed to PAHs or H_2 lines. The ratio of $6.2\text{-}\mu\text{m}$

to $7.7\text{-}\mu\text{m}$ intensities of the PAH features is 40 percent lower for PNe than for HII regions (Cohen et al. 1989, their Table 3) and this distinguishes the red false colour of PNe from the yellow of HII regions with PAHs.

Finally, the MIR/radio ratio is 42, again typical of UCHIs and much larger than the ratio for any group of PNe (e.g. Table 8, §9.1, and Paper-I). This, too, suggests that the object is, indeed a compact HII region and that the ambiguous nature of this object has finally been resolved.

Given that there are so many arguments against Hen 2-77 being a PN, one might wonder how there could have been so much confusion as to its character. The first description of its optical spectrum was by Henize (1954, 1967). Weak $\text{H}\alpha$ was seen and the line was “definitely widened relative to other nearby emission lines (‘diffuseness’ = 2)”. No continuum was detected even in a long exposure. These two criteria, applied to 95 PNe deemed to be well-confirmed, constituted the basis for its PN classification. Confirmation was further based on a resolved, reasonably regular, nebular image, however, no blue lines were recorded, probably due to the strong reddening. Henize stated the purity of his PN sample to be 97 per cent, but Westerlund & Henize (1967) described it as a “peculiar object” with a large bright knot on the west. In short, the classification rests solely on a weak $\text{H}\alpha$ emission line and the absent continuum, but the irregular image should have raised suspicion about the certainty of a PN classification.

The spectroscopic detection of moderately strong [OIII] emission was noted by Acker et al. (1992) and Kingsburgh & Barlow (1994) ([OIII]/ $\text{H}\beta \simeq 7$), which leads to the conclusion that this is a high-excitation compact HII region. The apparent presence of $\text{HeII } \lambda 4686$ emission noted by Shaw & Kaler (1989) suggests it may hold one or more embedded Wolf-Rayet stars.

2.2.2 Mz 3 “The Ant” nebula

The second ambiguous object is Mz 3, whose literature, by contrast, currently consists of 265 references in SIMBAD, almost 80 percent of which treat this unusual, highly collimated bipolar nebula as a planetary. The central core is unsaturated in IRAC and white in false colour, suggesting that warm dust emission is present, as found in many HII regions. However, this is also a characteristic of bipolar PNe that arises from the strong temperature gradients within their equatorial dust disks. The large dusty disk around Mz 3 was first identified by Cohen et al. (1978).

Fig. 3 shows Mz 3 in IRAC false colour, with the dense dust disk around the core in white (thermal emission by heated dust). The Spitzer diffraction spikes indicate the presence of a very compact, but unsaturated, central core.

Outside the bright core the putative PN is red in IRAC false colour. The polypolar PN NGC 6302 is in many ways similar to Mz 3, and so, by association, Mz 3 would also appear to merit the PN designation. It too has a large dust disk (Lester & Dinerstein 1984) and in MIR false colour its core is white and the surroundings are orange. The MIR/radio ratios are 23 for Mz 3 and 16 for NGC 6302. These values are well above the median for PNe (this paper) but very close to the median value (25 ± 5) for compact and diffuse HII regions (Cohen et al. 2007b). Another important aspect might also militate against assigning Mz 3 to PN status.

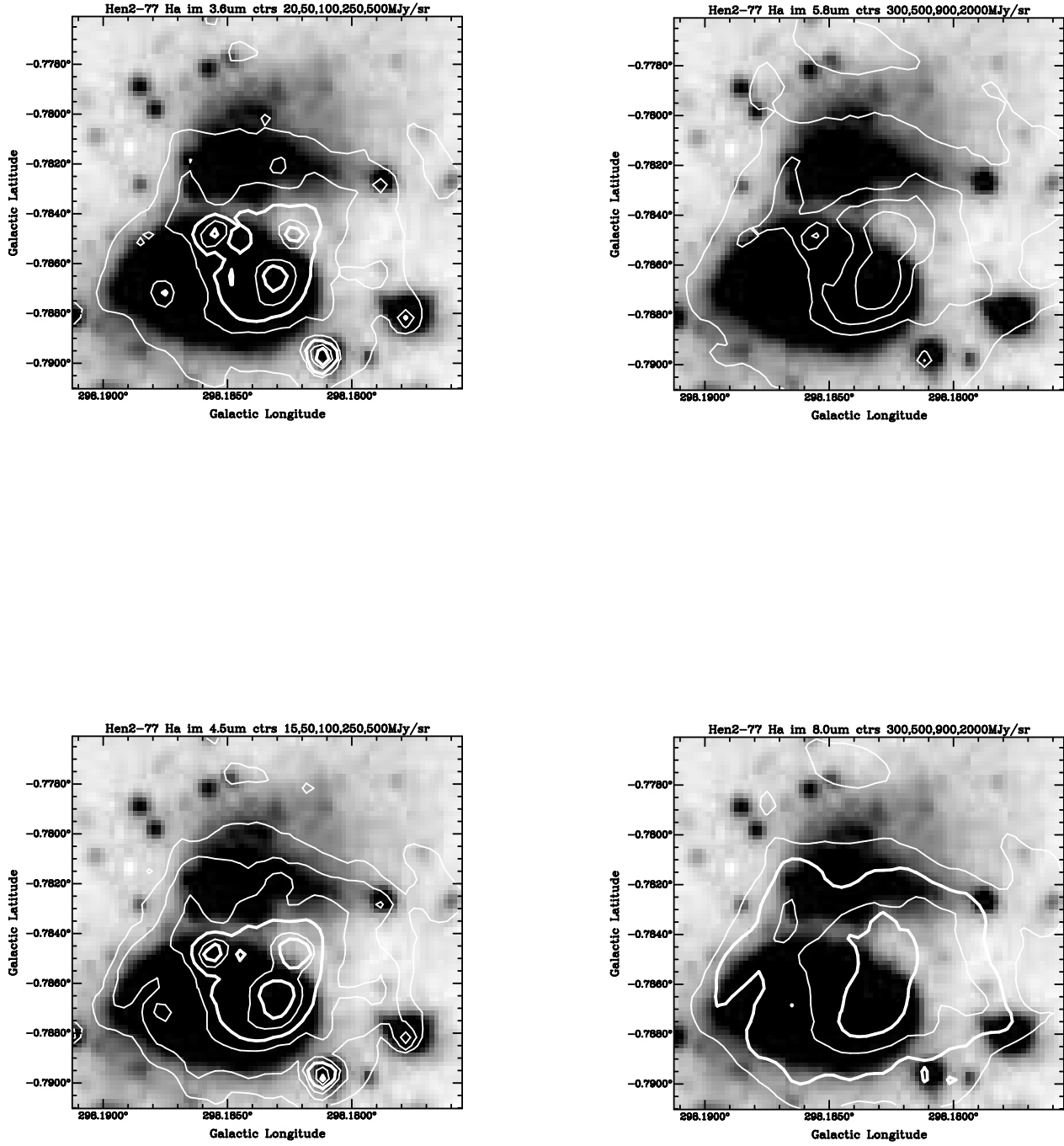


Figure 4. “Quartet” of IRAC MIR images in white contours overlaid on the grey scale H α image of Hen2-77. IRAC bands at 3.6, 4.5, 5.8, 8.0 μ m are overlaid in the top left; bottom left; top right; and bottom right positions. Note the dark lane (i.e. pale grey in the H α images) that divides the H α nebulosity into two separate pieces. For each IRAC band the white contour levels in MJy/sr are given at the top of the figures.

The 2MASS colours of the bright core of Mz 3 are $J - H = 2.00$, $H - K_s = 1.75$, locating it among the dusty symbiotic stars in the colour-colour plot of Corradi et al. (2008), although a few “true” PNe also share these colours. In §7 we shall see that Mz 3 is also highly anomalous in its optical emission line ratios. The possible analogue NGC 6302 is too extended to have reliable 2MASS photometry so it cannot be placed in the same NIR colour-colour plane. It is instructive to compare the spatially integrated absolute K-magnitudes of the most luminous known PNe with that of Mz 3, which has M_K in the range -6 to -7 , depending on the adopted distance (e.g. 1.6–2.5 kpc from the literature). By contrast, typical luminous PNe have M_K between -3 and -4 (e.g. Wainscoat et al. 1992, their Table 2). The bright, solar neighbourhood PN, NGC 7027, has M_K of -3.7 ; NGC 6302 -3.0 ; and even IR-[WC] PNe such as He 3-1333 have only $M_K \simeq -4$. The large, additional $2.2 \mu\text{m}$ luminosity in Mz 3 has been attributed to a cool AGB companion star (Smith 2003). Chesneau et al. (2007) find no evidence of a Mira companion, as suggested by Schmeja & Kimeswenger (2001), and prefer to associate Mz 3 with a young version of binary post-AGB stars. Mz 3 has also been considered as a link between D-type (dusty) symbiotic stars and PNe. For example Lutz et al. (1989) regard Mz 3, Hen2-104 and NGC 6302 as representing a small group of bipolar PNe which they argue are in transition from a PN to a symbiote. These authors identify low ionization objects like Mz 3 and M2-9 as having a dust torus still sufficiently opaque to prevent ionization of the outer disk, and in a phase preceding the high ionization PNe like NGC 6302. Santander-Garcia et al. (2008) find an unexpectedly large ionized gas mass of $0.1 M_\odot$ for Hen2-104. Yet Smith & Gehrz (2005) estimate the total mass of gas in Mz 3 as $0.6 M_\odot$. Consequently, Mz 3 is unusual even among those objects with which it has the closest affinity.

Frew & Parker (2010) relate objects like M 2-9 and Mz 3 to the symbiotic B[e] stars. While we cannot yet resolve the true nature of Mz 3, due to its non-conformist multi-wavelength characteristics, it seems prudent to exclude it from our previously known PN sample, especially as its MIR/radio ratio places it squarely in the regime of HII regions.

2.3 Other culled nebulae

The unique object G313.3+00.3 (Cohen et al. 2005) is culled because only extremely faint optical data are available for this highly obscured nebula that was discovered purely through radio and MIR observations, despite the fact that it is highly likely to be a *bona fide* PN (see footnote in §2). We have also eliminated several objects that have the appearance of bow shocks. Two of these are MASH candidate PHR1346-6116, and the previously known object PN G309.5+00.8. Such bow shocks might be associated with cataclysmic variables or simply represent random density enhancements in the diffuse ISM (Frew & Parker 2010: sec.4.10) that are ionized by nearby, reddened, hot, field stars that are passing through (Fig. 5). A large $8.0\text{-}\mu\text{m}$ arcuate structure in the ISM is indicated by the curving white contours from north to south in this field. This arc abruptly changes direction at the location of the $H\alpha$ nebulosity.

Without the often definitive and corroborating evidence of an optical spectrum no candidate can yet be treated as a *bona fide* PN. Consequently, we have not included any of the candidates offered by Phillips & Ramos-Larios (2008) that fall within our survey bounds although one or two, based solely on optical morphology, appear to be good PN candidates. It is possible that one might eventually be able to substitute NIR and/or MIR spectroscopy for

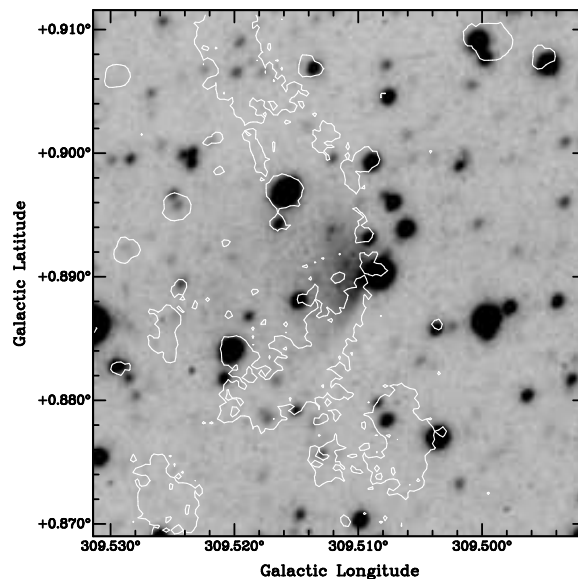


Figure 5. Rejected PN candidate PHR1346-6116: $H\alpha$ greyscale; white contours of $8.0 \mu\text{m}$ emission. The nebula is just visible as a faint diffuse darkening at the centre of the image, slightly east of the inflection in the diffuse $8.0\text{-}\mu\text{m}$ arc.

definitive optical spectral confirmation when obtaining the latter is problematic, due to a high level of extinction.

Note that many hundreds of IRAS sources have been suggested as potential PNe solely on the basis of their far-IR colours and they often lack any optical counterparts. However, the limited follow-up efforts to date have provided a very low yield of *bona fide* PNe. Suárez et al. (2006) pursued 253 IRAS source PN candidates but were able to confirm only 36 as PNe on the basis of optical spectroscopy. Ramos-Larios et al. (2009) have returned to IRAS sources but add NIR data to seek heavily reddened candidate PNe. No confirmed PNe are reported yet. Kwok et al. (2008) have also examined GLIMPSE images and presented a list of 30 objects which they assign to the status of PNe. Sixteen objects are indeed confirmed as such; 6 are in MASH and 10 are in the earlier literature. However, we believe that the remaining 14 nebulae are not in fact PNe. We are able to make this identification based on use of our new and existing discriminatory tools. Firstly, half of the objects we reject as PNe lack the critical verification through optical spectroscopy though we note seven had already been rejected by Parker et al. (2006) on the grounds of their morphology and optical spectra. Three of the sample were also explicitly identified as HII regions by Churchwell et al. (2006) in their catalogue of 322 thermal bubbles found in GLIMPSE. Another key point is that seven of the 14 objects we have rejected have very large integrated MIR flux densities at $8.0 \mu\text{m}$ ranging from 66 to 713 Jy which fall far outside the range found for confirmed Galactic PNe. Finally, several have angular areas of up to 60 arcmin^2 while only the very nearest PNe can attain such large angular sizes. All the above characteristics are highly typical of HII regions.

Yet, despite noting the very attributes that would normally exclude such objects as being identified as PNe in their paper, these authors gave these objects the PN G nomenclature for confirmed PNe.

It is just as important to delete such obvious contaminants from the on-line PN catalogues, based on improved understanding of their multi-wavelength characteristics, as it is to augment the literature by new members of the class. Therefore, we have included an appendix to the current paper which lists those objects we have identified in this study that should be removed from the extant catalogues and from SIMBAD as *bona fide* PNe. This list includes all 14 objects rejected from the Kwok et al. (2008) sample (being for the most part HII regions). We also urge the use of PN G names solely for confirmed PNe, following the accepted IAU convention. Note that our appendix rejects 25 objects, 16 percent of the 161 nebulae originally claimed as PNe in our observed area, the same proportion of non-PNe as Frew (2008) found for the local volume.

3 THE CLEAN SAMPLE OF PNE

After the culls and identity clarifications described above, we are left with 65 MASH-I, 30 MASH-II, and 41 PNe known prior to MASH, for a total of 136 PNe in this panchromatic study. Note that the 5 percent fraction of MASH PNe culled using our newly developed criteria, that now incorporate GLIMPSE MIR data, is lower than the 45 percent culled from the previously known PNe in our survey region. This reflects the care with which MASH catalogues were compiled and the heterogeneous nature of the pre-MASH catalogues which had not been subjected to our new discriminatory techniques as described by Frew & (Parker 2010). Note also that none of these culled MASH objects were designated as true PNe, rather having the designation of L (likely) or P (possible). We are now in a position to utilize our full armoury of multi-wavelength diagnostic tools in developing robust PN identification criteria based solely on MIR colours. Our cleaned PN sample has resulted from the application of our various diagnostic criteria and we believe it has minimal taint from the various kinds of PN mimic. We now proceed to examine their multi-wavelength properties with the emphasis on the predictive power inherent in the GLIMPSE MIR data and how to shape an identification scheme that can be applied in the absence of the traditional optical information.

Table 1 summarizes the attributes of MASH PNe. This single table contains the following information: Col. (1) – source name; Col. (2-3) – J2000 Equatorial coordinates with units shown; Col. (4-5) – Galactic coordinates in degrees; Col. (6) – status of the PN as true (T), likely (L), or possible (P); Col. (7) – optical dimensions in arcsec; and Col. (8) – optical morphology code, described below. Table 2 is similar but but for PNe known prior to MASH and carries both a common name and the PN G designation for each nebula.

Note that the PN designations as T (true), L (likely), or P (possible) follow the conventions adopted in MASH catalogues and encapsulate our current best understanding and interpretation of the object’s nature based on all the currently available data. Of course such designations are subject to change as improved, new, or different observational data come to light and it might become necessary to revise the status for a particular PN, especially for those objects with the P designation. PN dimensions for newly discovered objects are those determined by the MASH project from their SHS imagery and correspond to the main body of a given PN.

4 NEBULAR MORPHOLOGY

A detailed description of the morphological classifications of MASH PNe is given by Parker et al. (2006) and was utilized in Paper-I. We adopt the same basic scheme in the current paper. Note though, that in the absence of high-resolution CCD images, it is often difficult to provide definitive morphologies for small angular size PNe.

In this paper we investigate any correlation between optical morphologies and their MIR characteristics. The correlation between highly bipolar PNe and strongly enhanced He and N abundances is already well-known (e.g. Corradi & Schwarz 1995) but the original link between chemistry and morphology was noted by Greig (1967, 1971). Subsequently Peimbert (1978) and Peimbert & Serrano (1980) defined Type I PNe in terms of threshold values of He or N abundance. Throughout this paper, we define Type I PNe as having $N/O > 0.8$ following Kingsburgh & Barlow (1994). In other words, these PNe have experienced conversion, through envelope burning, of dredged-up primary carbon into nitrogen following the third dredge-up (Kingsburgh & Barlow 1994). It was found early on that most Type I PNe are bipolar (Peimbert 1978; Peimbert & Torres-Peimbert 1983), while later surveys of bipolar PNe (Corradi & Schwarz 1995) confirmed their chemical peculiarities and added enhanced Ne abundance to these.

Note however, that not all bipolar PNe have Type I chemistry. We have found a strong correlation between morphology and Type I chemistry, with the vast majority of Type I PNe having a bipolar morphology (Frew 2008; cf. Phillips 2005). However the inverse statement is not necessarily true, as many close-binary PNe show some evidence for bipolarity, but post-common envelope objects as a group tend to avoid Type I chemistries (De Marco 2009).

As a class, Type I PNe have larger than average diameters and expansion velocities (Corradi & Schwarz 1995), hotter and more massive central stars (Tylenda 1989), smaller Galactic scale heights (e.g. Stanghellini 2000), and tend to deviate more from the circular rotation of the Galaxy. Their association with more massive progenitors than typical PNe is widely acknowledged on theoretical grounds too (e.g. Becker & Iben 1980; Kingsburgh & Barlow 1994). This is consistent with the high proportion of new Type I PNe found by MASH at lower latitudes, and the larger fraction of round PNe found at high latitudes by MASH and later re-affirmed by the Deep Sky Hunter team in the Digital Sky Survey (Jacoby et al. 2010).

An intriguing correlation between bipolarity and the presence of 2.122- μ m H_2 emission in PNe was first noted by Zucker-man & Gatley (1988) and verified from a large sample of nebulae by Kastner et al. (1996). “Gatley’s rule” states that H_2 detection confirms the bipolar nature of a PN and represents the remnant of a pre-PN dusty molecular disk. Therefore, another objective of this paper is to seek quantitative differences between bipolar and non-bipolar PNe within the GLIMPSE survey which is already biased toward low latitude PNe with higher than average mass progenitor stars. For example, one might expect that PNe bright in the $v=1-0$ S(1) 2.122- μ m line might also be bright in the IRAC 4.5- μ m band due to emission from the strong $v=0-0$ S(9) 4.694- μ m line and this should be amenable to test by comparison of the observed IRAC colours of bipolar and non-bipolar PNe.

A homogeneous treatment of PN morphologies for the pre-MASH “known” objects, that is consistent with the above approach, has not been available because many objects from the Strasbourg ESO Catalogue: hereafter “SEC” (Acker et al. 1992, 1996),

Table 1. Attributes of MASH-I & MASH-II PNe

Name	RAJ2000	DecJ2000	GLON deg	GLAT deg	Status	Size arcsec	Morph. type
PHR1806–1956	18 06 55.3	–19 56 18	10.2111	0.3433	T	61×50	Bams
PHR1807–1827	18 07 11.7	–18 27 54	11.5293	1.0039	P	7×6	E
PHR1813–1543	18 13 29.0	–15 43 19	14.6575	1.0115	T	27×21	Eas
PHR1815–1457	18 15 06.5	–14 57 21	15.5185	1.0342	P	9×8	Es
PHR1818–1526	18 18 59.2	–15 26 22	15.5378	–0.0195	L	55×11	B
PHR1824–1505	18 24 02.1	–15 05 33	16.4158	–0.9312	T	30×18	Bps
PHR1821–1353	18 21 43.9	–13 53 13	17.2190	0.1272	P	20×6	As
PHR1826–0953	18 26 26.1	–09 53 26	21.2911	0.9803	T	54×42	Bs
PHR1831–0715	18 31 17.1	–07 15 23	24.1803	1.1436	P	19×15	Ias
PHR1831–0805	18 31 19.6	–08 05 43	23.4401	0.7449	L	13×9	Eas
PHR1834–0824	18 34 41.6	–08 24 20	23.5513	–0.1362	T	31×26	Ea
PHR1842–0539	18 42 17.9	–05 39 13	26.8632	–0.5529	L	90×65	Ias
PHR1842–0637	18 42 40.4	–06 37 02	26.0437	–1.0733	L	14×14	Ias
PHR1843–0541	18 43 10.4	–05 41 51	26.9222	–0.7630	T	48×39	B?/E
PHR1844–0517	18 44 54.0	–05 17 36	27.4764	–0.9616	L	122×68	Es!
PHR1838–0417	18 38 02.2	–04 17 24	27.5860	1.0186	P	15×13	Em
PHR1844–0503	18 44 45.7	–05 03 54	27.6643	–0.8265	T	35×12	Bm?/EM
PHR1844–0452	18 44 17.3	–04 52 56	27.7721	–0.6350	L	38×38	Rar
PHR1845–0343	18 45 06.0	–03 43 33	28.8931	–0.2907	L	51×30	B
PHR1843–0325	18 43 15.3	–03 25 27	28.9519	0.2570	P	10×9	Ea
PHR1842–0246	18 42 57.1	–02 46 01	29.5024	0.6246	L	24×13	Em
PHR1843–0232	18 43 56.9	–02 32 08	29.8197	0.5073	T	61×54	Ear
PHR1846–0233	18 46 02.7	–02 33 09	30.0485	0.0357	T	36×31	Ear
PHR1847–0215	18 47 47.4	–02 15 30	30.5060	–0.2200	T	20×14	Bs
PHR1850–0021	18 50 51.1	–00 21 30	32.5462	–0.0330	T	15×11	B
PHR1856+0028	18 56 51.1	+00 28 53	33.9770	–0.9860	L	8×7	Er
PHR1857+0207	18 57 59.5	+02 07 07	35.5650	–0.4910	L	11×11	Ea
PHR1150–6226	11 50 07.0	–62 26 32	295.9050	–0.4110	L	89×77	R
PHR1152–6234	11 52 55.7	–62 34 10	296.2510	–0.4580	L	27×24	R
PHR1157–6312	11 57 03.2	–63 12 44	296.8490	–0.9840	L	15×13	B?
PHR1202–6112	12 02 18.0	–61 12 47	297.0049	1.0958	T	14×13	Es
PHR1206–6122	12 06 25.5	–61 22 44	297.5680	1.0230	T	2×11	E
PHR1218–6245	12 18 00.9	–62 45 38	299.1190	–0.1360	L	42×31	Es
PHR1219–6347	12 19 08.2	–63 47 01	299.3720	–1.1353	L	22×17	Ea
PHR1220–6134	12 20 08.8	–61 34 16	299.2160	1.0747	L	10×9	Es
PHR1223–6236	12 23 58.0	–62 36 21	299.7780	0.0980	T	48×43	E
PHR1244–6231	12 44 28.5	–62 31 19	302.1330	0.3510	T	300×235	B
PHR1246–6324	12 46 26.5	–63 24 28	302.3730	–0.5390	T	31×19	B
PHR1250–6346	12 50 04.4	–63 46 52	302.7840	–0.9080	T	83×74	Ea
PHR1255–6251	12 55 18.0	–62 51 04	303.3725	0.0173	L	185×81	B
PHR1257–6216	12 57 51.3	–62 16 12	303.6783	0.5923	P	19×13	E
PHR1408–6229	14 08 47.3	–62 29 58	311.7300	–0.9500	T	82×46	B
PHR1408–6106	14 08 51.7	–61 06 27	312.1525	0.3741	T	307×264	Es
PHR1429–6043	14 29 52.8	–60 43 57	314.6780	–0.1290	P	167×131	E
PHR1429–6003	14 29 43.9	–60 03 17	314.9220	0.5180	L	141×110	E
PHR1432–6138	14 32 05.0	–61 38 42	314.5840	–1.0714	T	180×145	Es
PHR1437–5949	14 37 53.2	–59 49 25	315.9480	0.3320	T	103×63	Ba
PHR1447–5838	14 47 41.8	–58 38 41	317.5785	0.8845	P	57×65	I
PHR1457–5812	14 57 35.8	–58 12 09	318.9300	0.6930	T	31×25	A
PHR1507–5925	15 07 50.2	–59 25 14	319.5050	–1.0140	T	22×17	Ea
PHR1544–5607	15 44 56.7	–56 07 07	325.4480	–1.0270	P	14×10	E
PHR1552–5254	15 52 56.8	–52 54 12	328.3570	0.7670	T	31×26	Es
PHR1603–5402	16 03 41.4	–54 02 04	328.8410	–1.1311	L	40×21	A
PHR1610–5130	16 10 21.1	–51 30 54	331.2780	0.0600	P	20×11	Es
PHR1619–5131	16 19 57.6	–51 31 48	332.3493	–0.9814	P	11×11	E
PHR1622–5038	16 22 40.6	–50 38 42	333.2746	–0.6547	L	21×19	Ear
PHR1619–4914	16 19 40.1	–49 14 00	333.9279	0.6858	T	36×32	Rs
PHR1619–4906	16 19 50.1	–49 06 52	334.0350	0.7560	T	48×47	Ra
PHR1633–4650	16 33 58.0	–46 50 07	337.3141	0.6361	T	24×8	B
PHR1635–4654	16 35 51.9	–46 54 10	337.4831	0.3524	P	77×34	Ia/B?
PHR1634–4628	16 34 51.2	–46 28 28	337.6825	0.7684	T	22×17	E
PHR1639–4516	16 39 22.3	–45 16 35	339.0980	0.9880	T	38×25	Er

Table 1 continued

Name	RAJ2000	DecJ2000	GLON deg	GLAT deg	Status	Size arcsec	Morph. type
PHR1646–4402	16 46 27.6	–44 02 25	340.8600	0.8500	L	71×72	A
PHR1709–3931	17 09 10.8	–39 31 06	347.0320	0.3500	T	51×13	B
PHR1714–4006	17 14 49.3	–40 06 09	347.2000	–0.8720	T	20×11	B?
MPA1157–6226	11 57 47.52	–62 26 22	296.7712	–0.2110	T	12×5	E
MPA1235–6318	12 35 21.6	–63 18 01	301.1267	–0.4848	T	7×5	Eas
MPA1315–6338	13 15 30.2	–63 38 43	305.5994	–0.8984	T	6×6	R
BMP1322–6330	13 22 55.4	–63 30 34	306.4344	–0.8520	T	13×9	B
MPA1324–6320	13 24 16.8	–63 20 06	306.6067	–0.6978	T	10×10	Rr
BMP1329–6150	13 29 50.6	–61 50 39	307.4464	0.6908	T	87×72	Eas
MPA1337–6258	13 37 55.0	–62 58 54	308.1817	–0.5847	T	8×7	E
MPA1441–6114	14 41 32.2	–61 14 18	315.7823	–1.1440	T	7×6	E
BMP1522–5729	15 22 59.0	–57 29 59	322.1984	–0.4106	T	13×11	E
MPA1523–5710	15 23 22.5	–57 10 48	322.4178	–0.1720	T	35×6	Bms
BMP1524–5746	15 24 24.0	–57 46 22	322.2075	–0.7427	T	7 ×7	R
MPA1525–5528	15 25 06.1	–55 28 22	323.5573	1.1216	T	19×10	B/Ia
MPA1605–5319	16 05 37.4	–53 19 54	329.5234	–0.7963	T	8 ×6	E
MPA1618–5147	16 18 42.7	–51 47 45	332.0250	–1.0355	T	4 ×4	S
BMP1636–4529	16 36 58.7	–45 29 29	338.6580	1.1580	T	11 ×9	Em
MPA1713–4015	17 13 10.8	–40 15 56	346.8834	–0.7104	T	7 ×5	E
MPA1715–3903	17 15 16.1	–39 03 49	348.0937	–0.3334	T	78×72	Ra
MPA1717–3945	17 17 49.3	–39 45 58	347.8068	–1.1426	T	6×6	R
MPA1815–1602	18 15 21.2	–16 02 56	14.5852	–0.4614	L	6 ×5	Ea
MPA1819–1307	18 19 02.3	–13 07 04	17.5886	–1.0682	T	6 ×5	Ea/Bas?
MPA1822–1153	18 22 53.8	–11 53 10	19.1185	–0.8177	T	11×11	R
MPA1824–1126	18 24 04.1	–11 26 15	19.6493	–0.7741	T	13×12	Ear
MPA1827–1328	18 27 29.8	–13 28 19	18.2405	–0.9155	L	12×12	Rs
MPA1832–0706	18 32 22.8	–07 06 57	24.4297	0.9663	T	15×13	Emrs
MPA1840–0415	18 40 25.4	–04 15 34	27.8861	0.5029	T	15×6	Em
MPA1840–0529	18 40 49.2	–05 29 44	26.8326	–0.1517	T	7 ×5	E
MPA1843–0556	18 43 57.8	–05 56 20	26.7958	–1.0497	T	13×10	E
MPA1844–0454	18 44 49.7	–04 54 00	27.8184	–0.7663	T	7×7	S
MPA1851–0028	18 51 47.5	–00 28 29	32.5497	–0.2952	T	15×12	E
MPA1852–0044	18 52 24.2	–00 44 46	32.3778	–0.5549	T	5 ×5	R
MPA1852–0033	18 52 25.7	–00 33 27	32.5485	–0.4741	T	9 ×9	S

Table 2. Attributes of PNe known prior to MASH

Name	PN G	RAJ2000	DecJ2000 deg	GLON deg	GLAT	Status arcsec	Size type	Morph.
Hen 2-83	300.2+00.6	12 28 43.9	-62 05 35	300.279	0.662	T	4.5×4.5	E
Hen 2-84	300.4-00.9	12 28 46.8	-63 44 36	300.429	-0.982	T	36×24	B
Hen 2-85	300.5-01.1	12 30 07.7	-63 53 01	300.589	-1.109	T	9×8	E
Wray16-121	302.6-00.9	12 48 31.2	-63 50 04	302.610	-0.965	T	65×54	Es
TH 2-A	306.4-00.6	13 22 33.8	-63 21 02	306.414	-0.689	T	27×25	Epr
WKG2	308.4+00.4	13 38 42.7	-61 55 47	308.462	0.433	T	38×32	Er
Hen 2-96	309.0+00.8	13 42 36.2	-61 22 29	309.021	0.891	T	17×14	E
...	313.3+00.3	14 18 27.8	-60 47 10	313.355	0.312	P	28×28	R
Hen 2-111	315.0-00.3	14 33 18.0	-60 49 37	315.030	-0.371	T	29×15	Bmp
GLMP387	316.2+00.8	14 38 19.9	-59 11 46	316.247	0.884	P	6.5×5.5	S
Pe2-8	322.4-00.1	15 23 43.0	-57 09 25	322.469	-0.178	T	1.9×1.3	S
GLMP437	327.8-00.8	15 57 21.1	-54 30 46	327.829	-0.888	P	6.5	S
Hen 2-145	331.4+00.5	16 08 58.8	-51 01 58	331.448	0.562	T	17×15	B
Mz 3	331.7-01.0	16 17 13.4	-51 59 11	331.727	-1.011	P	48×23	B
Hen 2-169	335.4-01.1	16 34 13.2	-49 21 13	335.492	-1.103	T	22×19	Bs
H 1-3	342.7+00.7	16 53 31.2	-42 39 22	342.744	0.752	T	20×16	B
GLMP495	342.2-00.3	16 56 34.1	-43 46 14	342.226	-0.380	P	7.5	S
H 1-5	343.9+00.8	16 57 23.8	-41 37 58	343.992	0.835	T	69×5	E
HaTr 5	343.3-00.6	17 01 28.6	-43 05 57	343.305	-0.664	T	120×110	Rar
IC4637	345.4+00.1	17 05 10.6	-40 53 08	345.479	0.140	T	19×14	Eap
NGC6337	349.3-01.1	17 22 15.7	-38 29 03	349.3510	-01.116	T	48×42	Erspm
NGC6302	349.5+01.0	17 13 44.4	-37 06 16	349.5075	-1.016	T	90×35	Bs
NGC6537	010.1+00.7	18 05 13.0	-19 50 35	10.0987	0.740	T	11×10	Bmps
Sab39	011.7+00.2	18 10 19.7	-18 39 10	11.7255	0.264	T	17×12	E
NGC6567	011.7-00.6	18 13 45.1	-19 04 35	11.7433	-0.650	T	8×6	Ep
M1-43	011.7+00.0	18 11 48.9	-18 46 22	11.7898	-0.102	T	15×12	S
M3-53	019.9+00.9	18 24 07.9	-11 06 42	19.9447	0.912	L	10×9	S
PM 1-231	020.4+00.6	18 25 58.1	-10 45 29	20.468	0.679	L	9×7	S
PM 1-235	021.6+00.8	18 27 45.6	-09 38 13	21.6656	0.811	P	2.5	S
GLMP781	021.1+00.4	18 28 01.2	-10 14 08	21.1654	0.476	P	6.5×5.5	S
Abell45	020.2-00.6	18 30 15.6	-11 37 02	20.1965	-0.652	L	300×280	Ers
Mac 1-13	022.5+01.0	18 28 35.3	-08 43 22	22.5699	1.055	T	23×17	E/B
M3-28	021.8-00.4	18 32 41.3	-10 05 52	21.8197	-0.478	T	24×12	Bp
M3-55	021.7-00.6	18 33 14.9	-10 15 20	21.7431	-0.673	T	12×9	B
M1-51	020.9-01.1	18 33 29.04	-11 07 27	20.9991	-1.125	T	15×8	B
M2-45	027.7+00.7	18 39 21.8	-04 19 51	27.7017	0.705	T	15×12	E
Pe 1-14	025.9-00.9	18 42 07.9	-06 40 55	25.9269	-0.984	T	13×10	B
Abell48	029.0+00.4	18 42 46.8	-03 13 16	29.0786	0.455	T	50×43	Em
TDC 1	029.2+00.0	18 44 53.5	-03 20 33	29.2111	-0.069	L	6×5	E
HaTr 10	031.3-00.5	18 50 24.5	-01 40 19	31.3267	-0.534	T	34×28	B
WeSb4	031.9-00.3	18 50 40.3	-01 03 13	31.9067	-0.310	T	69×42	B
CBSS3	032.9-00.7	18 54 06.7	-00 20 02	32.9396	-0.748	T	7×5	E
GLMP844	033.4-00.6	18 54 34.80	00 11 04.6	33.4544	0.615	T	3.5	S

One GLIMPSE detected nebula in Table 2, G313.3+00.3 (Cohen et al. 2005), has no common name in col.(2) because its optical counterpart is too faint to characterize the nebula.

Table 3. Derived data for all our samples of PNe

Name	[3.6]	1–2	1–3	1–4	2–3	2–4	3–4	False colour	H α /[SII] log ₁₀	H α /[NII] log ₁₀	N _e ([SII] cm ^{−3}	MOST/ NVSS	Radio mJy	8.0 μ m mJy	MIR/Radio
PHR1150–6226	9.70	0.60	1.81	2.35	1.21	1.74	0.54	X
PHR1152–6234	1.09	1.67	0.58	X	0.13	−0.11
PHR1157–6312	12.88	1.72	2.37	4.42	0.65	2.69	2.05	R	0.44	−0.35	700	m	6.4	22	3.5
PHR1202–6112	2.84	...	u	0.05	−0.79	180	m	8.3	10.6	1.3
PHR1206–6122	14.19	1.50	2.25	2.72	0.75	1.21	0.47	V	0.55	0.14	150
PHR1218–6245	u	0.28	−0.28	130
PHR1219–6347	12.32	0.14	2.25	2.76	2.11	2.63	0.52	O	...	−0.16	...	m	230	7.8	0.03
PHR1220–6134	1.43	...	u	0.88:	0.05	...	m	9.4	8.7	0.9
PHR1223–6236	11.50	−0.31	0.34	1.60	0.64	1.89	1.26	X	0.53	−0.24
PHR1244–62313.34	4.25	0.91	X	0.18	−0.89	100
PHR1246–6324	11.05	0.63	2.49	4.27	1.85	3.64	1.79	R	0.90	0.10	850	m	14	100	7.4
PHR1250–6346	1.46	3.29	1.85	X	0.37	−0.26	150
PHR1255–6251	0.51	−1.68	−2.18	X	−0.13	−1.18
PHR1257–6216	12.24	0.21	0.82	2.14	0.61	1.94	1.33	V
PHR1408–6106	9.82	u	0.28	−0.28	130
PHR1408–6229	13.19	2.44	u	0.27	−0.75
PHR1429–6003	9.53	1.63	3.02	4.39	1.42	2.78	1.37	X	−0.16	−0.71	10
PHR1429–6043	8.46	0.68	2.73	4.25	2.04	3.56	1.53	X
PHR1432–6138	9.03	−1.12	1.46	4.70	2.58	5.82	3.24	X	0.23	−0.43	270
PHR1437–5949	9.21	0.78	0.89	3.23	0.11	2.44	2.34	R	0.03	−0.91	...	m	12	240	20
PHR1447–5838	3.33	...	u	0.41	0.07	270
PHR1457–5812	10.48	0.20	1.29	3.75	1.09	3.54	2.46	R	0.46	−0.55	1500	m	80	120	1.5
PHR1507–5925	10.56	0.88	1.74	3.01	0.86	2.12	1.27	V	0.83	0.45	900	m	24	74	3.6
PHR1544–5607	0.54	3.34	2.81	X	−0.07:	−0.12:
PHR1552–5254	10.60	0.65	1.38	3.80	0.74	3.14	2.42	R	0.37	−0.41	600	m	21	100	4.4
PHR1603–5402	3.41	...	u	0.39	0.39
PHR1610–5130	13.19	0.17	u	0.51	0.08	400
PHR1619–4906	2.39	4.43	2.05	X	−0.63
PHR1619–4914	8.78	0.93	1.02	3.14	0.10	2.22	2.12	R	0.87	−0.41	1300	m	240	720	3.0
PHR1619–5131	11.51	0.18	2.44	4.15	3.16	4.95	1.80	V	m	20	73	3.6
PHR1622–5038	11.13	1.69	2.46	4.01	0.77	2.31	1.55	V	0.52	0.24
PHR1633–4650	2.74	4.62	1.90	O	0.03	−0.88	400	m	27	47	1.7
PHR1635–4654	u
PHR1634–4628	11.77	1.06	2.09	3.42	1.03	2.35	1.33	X	0.17	−0.19	60
PHR1639–4516	9.62	1.52	−0.07	...	1.11	u	0.49	−0.31	70
PHR1646–4402	10.21	−0.54	0.47	1.51	1.00	2.03	1.04	X	...	−0.64
PHR1709–3931	14.70	2.89	6.57	7.24	3.68	4.34	0.67	X	0.02	−0.88
PHR1714–4006	12.59	1.47	3.09	3.93	1.62	2.45	0.84	R	0.52	−0.46	...	m	9.7	20	2.1
PHR1806–1956	11.55	...	3.47	4.67	2.73	u	0.28	−0.50	700
PHR1807–1827	17.13	3.38	4.74	6.92	1.38	3.54	2.17	X	0.11
PHR1813–1543	1.77	u	0.65	0.19
PHR1815–1457	3.18	...	u	n	9.2	12	1.3
PHR1818–1526	9.80	1.53	3.37	1.41	1.84	−0.13	−1.96	X	0.20	−0.70	250
PHR1824–1505	12.94	1.57	3.10	1.19	1.53	−0.39	−1.91	X	0.46:	−0.50	80:
PHR1821–1353	11.36	u	1.3
PHR1826–0953	9.77	0.56	2.45	3.92	1.66	3.36	1.46	X	0.33	−0.33	170	n	8.4	130	15
PHR1831–0715	2.14	...	u	...	0.29	...	n	5.9	21	3.6

Name	[3.6]	1–2	1–3	1–4	2–3	2–4	Table 3 continued		$H\alpha/[SII]$ \log_{10}	$H\alpha/[NII]$ \log_{10}	$N_e([SII])$ cm^{-3}	MOST/ NVSS	8.0 μm mJy	Radio mJy	MIR/Radio
							3–4	False colour							
PHR1831–0805	12.20	0.50	1.93	3.70	1.43	3.18	1.76	V	0.25	−0.49	2800
PHR1834–0824	11.95	u
PHR1838–0417	−0.06	1.99	2.67	V	...	1.15
PHR1842–0246	10.55	0.36	−2.23	−0.15	−1.98	...	2.08	R	...	−0.58
PHR1842–0539	8.52	0.29	1.19	2.41	1.29	2.51	1.23	X	−0.26	−1.25	1000
PHR1842–0637	10.36	−0.08	−0.07	0.61	0.01	0.69	0.68	V	−0.84
PHR1843–0232	8.46	1.13	3.18	5.02	2.05	3.88	1.84	X	0.50	−0.18	...	n	33	700	21
PHR1843–0325	11.30	1.10	2.71	4.66	1.60	3.55	1.94	V	...	0.38	...	n	16	160	10
PHR1843–0541	−1.04	0.00	1.09	X	0.09	−0.90	400
PHR1844–0452	10.20	0.58	1.71	1.34	1.17	0.78	0.38	X	0.29	−0.75	500
PHR1844–0503	12.06	0.80	1.86	2.98	1.05	2.20	1.38	O	0.81	−0.36	2500	n	3.2	58	18
PHR1844–0517	11.49	−2.08	0.54	2.42	2.62	4.48	1.88	X	0.47	−0.66
PHR1845–0343	9.16	0.64	1.07	2.70	1.10	3.01	1.91	O	...	−0.84
PHR1846–0233	1.67	...	u	...	−0.38
PHR1847–0215	10.40	...	1.69	3.95	5.26	7.51	2.21	V	0.57	−0.61
PHR1850–0021	12.83	0.88	1.03	2.99	0.18	2.15	1.97	X	−0.42	n	5.0	7.4	1.5
PHR1856+0028	11.83	0.21	0.74	2.64	0.35	2.17	1.91	V	0.61	−0.04	750
PHR1857+0207	10.40	0.67	1.47	3.48	0.81	2.82	2.00	R	...	0.51	...	n	100	130	1.3
MPA1157–6226	12.72	0.71	1.37	2.25	0.66	1.55	0.89	R	0.46	−0.73	300
MPA1235–6318	13.91	1.60	2.06	3.93	0.46	2.34	1.88	O	0.32	−0.49	650
MPA1315–6338	11.35	0.38	1.24	2.83	0.86	2.45	1.59	O	0.52	−0.23	630	m	4.9	25	5.0
BMP1322–6330	13.36	0.31	1.53	3.21	1.22	2.90	1.67	O	−0.11	−1.15	90	m
MPA1324–6320	13.32	0.61	1.06	2.83	0.45	2.22	1.77	R	0.37	−0.24	500	m
BMP1329–6150	11.39	1.67	2.24	4.74	0.57	3.07	2.50	X	...	−0.48	...	m
MPA1337–6258	12.20	0.69	1.11	2.50	0.42	1.81	1.39	R	0.93:	−0.31	800:
MPA1441–6114	11.32	0.95	1.13	2.85	0.17	1.89	1.72	R	2.06:	1.31:	60	m	20	26	1.3
BMP1522–5729	11.10	1.25	1.78	3.99	0.53	2.74	2.21	R	0.85	−0.35	3600	m	17	90	5.2
MPA1523–5710	12.18	1.78	2.25	4.14	0.48	2.36	1.88	R	0.47	−0.66	1300	m	27	38	1.4
BMP1524–5746	9.63	0.84	1.35	3.17	0.52	2.33	1.82	R	0.71	−0.19	2100	m	27	170	6.1
MPA1605–5319	11.78	0.87	1.90	3.75	1.03	2.88	1.85	O	0.92	−0.05	2000	m	5.1	39	7.6
MPA1618–5147	12.60	0.39	0.26	1.86	−0.13	1.47	1.61	V	0.84	−0.34	470
BMP1636–4529	2.83	u	0.97	−0.18	1300	m	22	60	2.7
MPA1713–4015	11.12	0.69	2.02	4.06	1.34	3.37	2.04	O	0.83	−0.18	2000
MPA1715–3903	9.67	2.75	1.95	3.70	−0.80	0.95	1.75	X	0.47	−0.17:	300
MPA1717–3945	12.41	...	1.29	u	...	1.09	...	m
MPA1815–1602	11.67	1.61	2.09	4.08	0.48	2.47	1.99	O	0.43	−0.53	1400	n	11	28	2.6
MPA1819–1307	13.79	1.95	1.70	4.51	−0.13	2.56	2.82	R	...	1.20	...	n	5.2	12	2.4
MPA1822–1153	11.86	0.70	0.75	2.68	0.06	1.98	2.68	R
MPA1824–1126	11.11	0.28	−0.62	1.32	−0.91	1.04	1.94	V	1.10:	0.88	700:
MPA1827–1328	10.77	1.86	1.46	3.09	−0.40	1.23	1.63	R	0.41:	0.24?	...	n	34	54	1.6
MPA1832–0706	10.17	0.28	2.01	3.83	1.72	3.55	1.83	O	0.88	−0.10	1100	n	5.5	210	38
MPA1840–0415	12.38	0.81	1.04	2.34	0.23	1.52	1.30	R	0.42	−0.73	4500
MPA1840–0529	12.03	0.90	1.03	2.98	0.13	2.08	1.96	V	0.26:	−0.48	800:	n	1.4	15	11
MPA1843–0556	11.40	0.32	0.20	2.17	−0.12	1.84	1.97	O	0.40	−0.50	1400	n	5.5	13	2.3
MPA1844–0454	12.68	0.74	0.84	2.84	0.10	2.10	2.00	O	0.82:	−0.59	2400:
MPA1851–0028	12.23	1.29	1.39	3.80	0.10	2.51	2.41	O	0.35	−0.47	140
MPA1852–0044	13.59	0.68	1.85	3.86	1.17	3.19	2.01	R	...	−0.47
MPA1852–0033	9.87	0.69	1.78	3.81	1.09	3.12	2.03	O	1.37	0.12	24000	n	20	240	12

Table 3 continued

Name	[3.6]	1–2	1–3	1–4	2–3	2–4	3–4	False colour	H α /[SII] log ₁₀	H α /[NII] log ₁₀	N _e ([SII] cm ⁻³	MOST/ NVSS	Radio mJy	8.0 μ m mJy	MIR/Radio
Hen 2-83	9.84	0.91	1.56	3.87	0.65	2.96	2.31	R	1.23	-0.16	7000	m	41	260	6.4
Hen 2-84	11.15	1.31	2.07	2.94	0.76	1.63	0.87	R	0.44	-0.38	850	m	12	33	2.8
He 2-85	10.18	1.61	1.06	2.90	-0.55	1.29	1.83	R	1.32	0.54	3400	m	77	78	1.0
Wray16-121	13.08	0.24	1.33	3.52	1.09	3.28	2.19	X	0.24	-0.73	1100	m	27	300	11
TH 2-A	9.26	-0.13	1.12	3.26	1.25	3.39	2.14	R	1.21	0.26	1000	m	16	250	16
WKG2	11.45	1.00	1.67	4.19	0.67	3.18	2.51	X	0.87	-0.29	140
Hen 2-96	9.17	0.52	2.11	4.12	1.58	3.59	2.01	O	1.58	0.47	8300	m	17	600	35
Hen 2-111	7.68	2.20	3.49	25.82	1.29	3.62	0.63	O	0.26	-0.78	700	m	82	870	11
GLMP387	9.18	0.82	2.07	4.21	1.25	3.39	2.14	O	m	13	650	49
Pe2-8	8.27	1.08	1.90	4.34	0.83	3.26	2.43	R	2.12	0.66	11000	m	27	1700	62
GLMP437	9.75	0.61	1.76	3.81	1.15	3.20	2.05	O	m	62	260	4.2
Hen 2-145	9.82	0.52	3.15	4.84	2.62	4.31	1.69	X	...	-0.37	...	m	58	640	11
Hen 2-169	10.26	1.21	2.06	4.37	0.85	3.16	2.32	O	0.28	-0.76	1400	m	97	280	2.9
H 1-3	9.32	0.11	0.99	2.57	0.88	2.45	1.57	R	0.28	-0.54	500	m	32	120	3.9
GLMP495	9.30	1.26	1.16	2.91	-0.10	1.64	1.75	R	1.31	0.60	3900	m	76	180	2.3
H 1-5	8.64	0.99	1.53	3.70	0.55	2.72	2.17	R	1.26	0.29	24000	m	115	670	5.8
HaTr5	8.69	-0.14	1.89	4.21	2.03	4.35	2.32	X
IC4637	8.67	0.84	1.52	2.47	0.68	1.63	0.95	O	...	1.23	...	m	210	210	1.0
NGC6337	u	0.22	-0.80	260	m	106
NGC6302	6.04	1.59	2.56	4.82	0.97	3.23	2.26	O	0.90	-0.36	5400	m	1200	20000	16
NGC6537	7.33	1.29	2.35	4.40	1.06	3.11	2.05	O	0.87	-0.14	...	n	430	4300	10
Sab39	12.08	2.40	0.88	3.86	-1.51	1.46	2.98	R	0.82	0.04	1100	n	13	33	2.5
NGC6567	8.03	0.70	1.76	4.10	1.07	3.41	2.34	O	2.28	1.36	11000	n	160	1700	10
M1-43	9.94	0.63	-0.21	1.95	-0.84	1.32	2.16	V	...	1.00
M3-53	10.55	0.75	1.76	3.87	1.00	3.11	2.11	O	0.68	-0.32	3200	n	20	130	6.9
PM 1-231	10.40	1.23	1.69	4.08	0.46	2.85	2.39	R	1.25:	0.09	3900:	n	49	190	3.9
PM 1-235	9.90	1.23	2.67	4.54	1.44	3.31	1.87	O	n	16	450	28
GLMP781	8.18	0.84	2.17	4.28	1.34	3.45	2.11	R	n	38	1700	46
Abell45	2.30	u
Mac 1-13	10.82	1.29	1.46	3.61	0.17	2.32	2.15	R	0.33	-0.40	1100	n	30	82	2.7
M3-28	9.13	0.81	2.36	4.05	1.56	3.24	1.68	R	1.12	-0.34	1400	n	20	590	30
M3-55	11.32	-0.03	1.52	3.27	1.55	3.30	1.75	R	0.60	-0.50	1700
M1-51	8.06	...	0.58	u	1.12	-0.24	11000	n	250
M2-45	9.64	1.02	0.18	3.27	-0.84	2.24	3.09	V	1.24	0.39	3200	n	110	180	1.7
Pe 1-14	12.52	1.34	2.02	3.68	0.68	2.34	1.66	R	0.46	-0.42	1150	n	2.2	18	8.4
Abell48	9.55	1.59	0.67	3.50	-0.92	1.92	2.83	R	1.32	0.58	240	n	160	240	1.5
TDC 1	9.41	0.93	1.73	3.96	0.80	3.03	2.23	R	n	140	420	3.0
HaTr 10	11.11	0.51	0.93	1.95	0.42	1.45	1.03	V	0.22	-0.80	260
WeSb4	10.04	1.15	1.30	2.82	0.15	1.67	1.53	V	0.20	-0.90	550	n	4.3	82	19
CBSS3	11.86	0.69	1.38	3.13	0.69	2.44	1.75	O	0.35	-0.49	900	n	2.0	20	810
GLMP844	8.71	0.79	2.35	4.40	1.56	3.61	2.05	R	...	-0.10:	...	n	6.5	1200	180

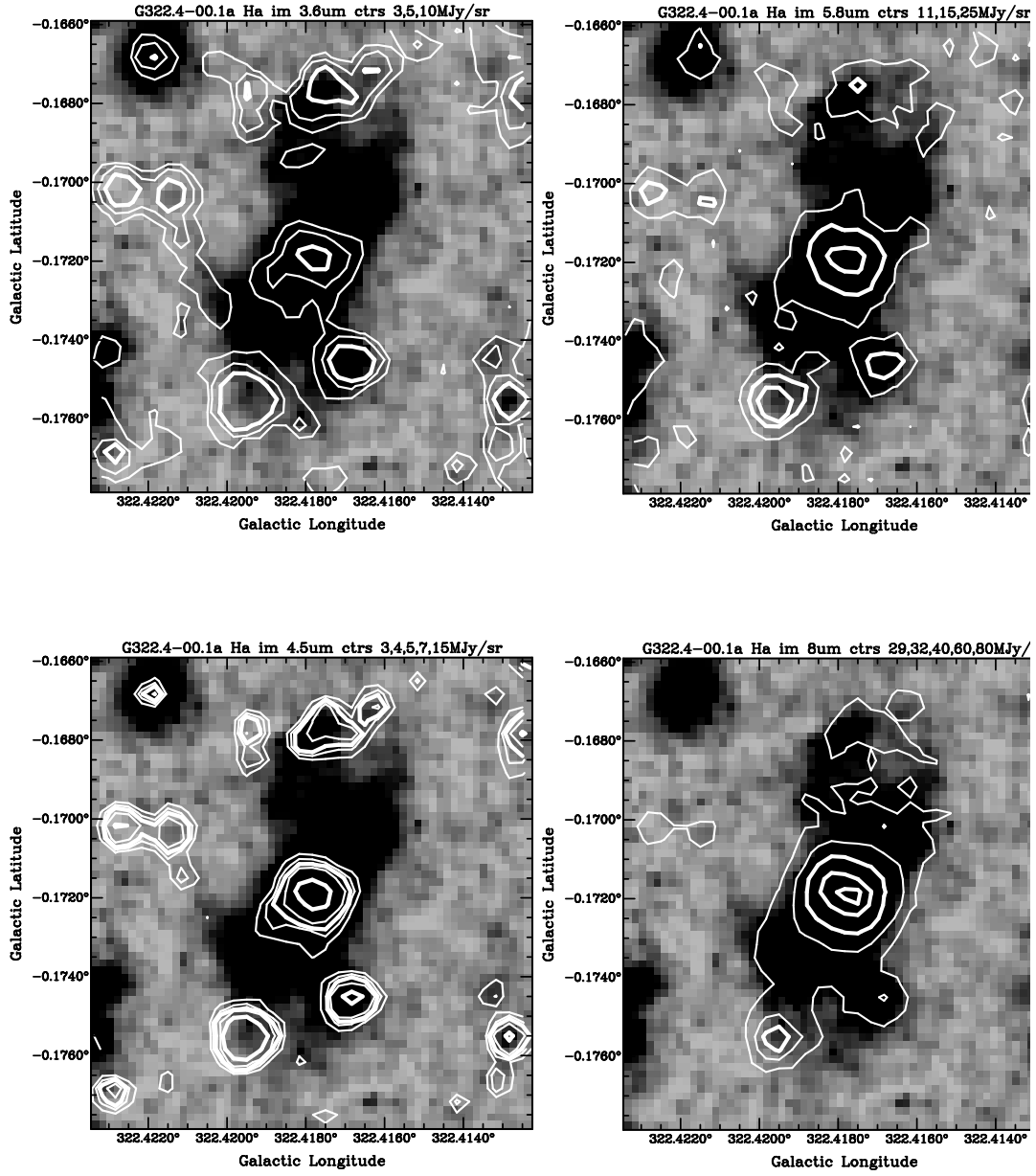


Figure 6. Quartet of MASH-II PN, PN G322.4-00.1a (MPA 1523-5710). The nebula is bipolar in $\text{H}\alpha$ (greyscale image). At short wavelengths (3.6 μm [top left]) and (4.5 μm [bottom left]) the central star dominates. This star, and/or the nebula centre, brightens at (5.8 μm [top right]) and (8.0 μm [bottom right]). Diffuse 8.0- μm emission is also detected along the major axis of the nebula

lacked images at high resolution. However, the importance of having a well-defined set of PNe believed to be bipolar, to contrast with round nebulae, was motivation for us to re-examine all available CCD images for known PNe via the catalogues of PN images by Manchado et al. (1996) and Balick (2008,2009) in order to characterize them. Table 2 offers a characterization of these nebulae using the identical scheme as for MASH nebulae. For starlike, unresolved PNe, we indicate simply an “S” as no morphological type can be extracted. For resolved SEC nebulae the sizes were taken preferentially from Tytenda et al. (2003) who measured them at the 10 percent isophotal level, or from Ruffle et al. (2004). When necessary, we measured SEC nebular diameters to the 10 percent level ourselves, comparing the SHS (Parker et al. 2005), $H\alpha$ and Short Red sizes. In the case of very small or optically faint PNe we took the IRAC 8.0- μ m dimensions.

Both MASH-I and MASH-II PNe are very similar in their MIR appearance. For example, in Fig. 6 we present a quartet of IRAC images for MASH-II bipolar object MPA1523-5710 (PN G322.4-00.1) overlaid on the greyscale SHS $H\alpha$ image of this nebula. In Paper-I we illustrated several examples of such quartets to show the changing morphology with IRAC wavelength. The central star dominates the nebular core at short wavelengths, brightening and growing in size at longer wavelengths as do many PNe that show the PAH emission features. Note that diffuse emission is also detected at 8.0 μ m, along the major axis of the nebula.

5 PNE OF LARGE ANGULAR SIZE

Both MASH-I and MASH-II include significant numbers of PNe with large angular size, but these are predominantly of much lower surface brightness than pre-MASH nebulae. Large angular size PNe are well-resolved so that we can trace the variations in dominant MIR emission across the nebulae by MIR false colour changes. These PNe are of low surface brightness but are close to the sun and so appear with large angular extent. They typically lack PAH emission, perhaps because these lower density nebulae are optically thin to ionizing radiation and their nuclei no longer furnish enough UV radiation to maintain easily detectable PDRs. Although IRAC surveys of PNe (e.g. Hora et al. 2004) do readily detect nearby, high surface brightness optical PNe of large angular size, we found a dearth of MIR detections of large nebulae in Paper-I. We concluded that the large angular MASH-I PNe in which PAHs have been detected are bipolar, high-excitation PNe, in which PAHs are found in a high-density central circumstellar disk. We emphasize the fact that all large nebulae do not necessarily present the same MIR emission process, and offer two examples to demonstrate this.

5.1 Abell 48

Fig. 7 shows the 50'' diameter PN G029.0+00.4 (Abell 48), almost all of whose interior is red in false colour. This image also serves as a paradigm for a PN that stands out against the local ISM. There are red regions elsewhere in Fig. 7 but these are clearly amorphous (e.g. the NW corner and W side of the box) or local diffuse orange patches (e.g. the N edge of the frame). But this PN contrasts with everything else in the overall image by its red color which traces the entire extent of this PN. It is also of interest because it seems to be a member of the group of PNe with Wolf-Rayet central stars, (DePew et al. 2010), perhaps even of the rarer subset of [WC/WN]

PNe (Morgan, Parker & Cohen (2003); Todt et al. (2010). Then one would expect the red nebular false colour to be PAH emission rather than H_2 because the C-rich aspect of dual-dust PNe is shown by strong PAH bands.

5.2 Hen 2-111

By contrast, PN G315.0-00.3 (Hen 2-111: Webster et al. 1978) consists of a bright central body (29×15 arcsec), surrounded by a huge bipolar filamentary halo of emission over 10 arcmin in extent that is expanding at substantial velocities of order 500 km s^{-1} (Meaburn & Walsh (1989). While these are all unusual characteristics for a PN, this object is still regarded as a bona-fide PN. MIR emission from heated dust (false colour white) is seen to be associated solely with the bright core (Fig. 8). The object lies in a region of the ISM with very complex structure but no other obviously associated MIR features appear within the optical extent of the nebula. The extensive network of $H\alpha$ filaments in the outer halo is represented by the black overlaid contours.

PN G315.0-00.3 offers an opportunity to compare the MIR colours of a bright PN core with those of the whole nebula. The six IRAC colours (as presented in Table 3) for the entire nebula are (1.36, 1.74, 2.37, 0.38, 1.02, 0.63) but the bright compact core has (2.20, 3.49, 5.82, 1.29, 3.62, 2.34), presenting a substantially different MIR character. This implies sizeable spatial variations in the mix of emission processes across the PN. Such processes will include PAH molecular bands, H_2 emission lines, fine structure lines, atomic recombination lines, thermal emission from dust species, such as silicates, both amorphous and crystalline, carbon, and SiC, and species without any obvious MIR features, such as graphite. On the basis of longer wavelength comparisons of Spitzer 24- μ m and $H\alpha$ images of PNe, Chu et al. (2009) argued that the relative contributions of fine structure lines and dust emission vary from nebula to nebula. Hora et al. (2004) have observed that, even within a single PN, different MIR emission processes occur in different spatial regions.

6 ANALYSIS OF THE CLEAN SAMPLE OF PNE

Table 3 contains all our derived and collateral data on each PN that has passed our careful selection criteria. This information consists of the following: after the designation of a PN (col.1) we give the [3.6], the IRAC 3.6- μ magnitude, the IRAC colour indices in Vega-based magnitudes (cols.3-8). col(9) contains the IRAC 4.5-5.8-8.0 μ m (blue, green, red) false colour if the nebula stands out against the background. Cols.(10-11) present two optical emission-line flux ratios: $\log_{10} H\alpha/[SII]$ (col.10) and $\log_{10} H\alpha/[NII]$ (col.11); the electron density N_e derived from the [SII] optical emission line ratios from the available spectroscopy appears in (col.12); (note we have 100 percent spectral coverage for all MASH PNe); whether a PN has radio continuum emission “m” from Molonglo at 843 MHz or “n” from the NVSS at 1.4 GHz is noted in (col.13); if so then the radio flux density is given in (col.14); the 8.0- μ m IRAC flux density appears in (col.15); if both MIR and radio detections are available then the ratio of MIR/radio flux densities is noted in (col.16). Our optical emission-line database was assembled from homogeneous observations with the Flames spectrograph at the VLT, the 2DF and AAOmega instruments on the 3.9m Anglo-Australian Telescope, the Double Beam Spectrograph at the ANU 2.3m telescope, FLAIR on the UK Schmidt Telescope, and the grating spectrograph on the

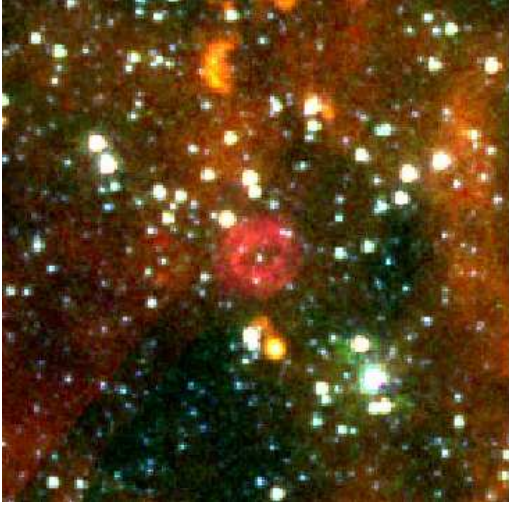


Figure 7. PN G029.0+00.4 (Abell 48) has a 50 arcsec diameter in $H\alpha$ and MIR emission is clearly seen across the entire nebular extent. this PN is very clearly distinguished from the surrounding ISM by both false colour and shape.

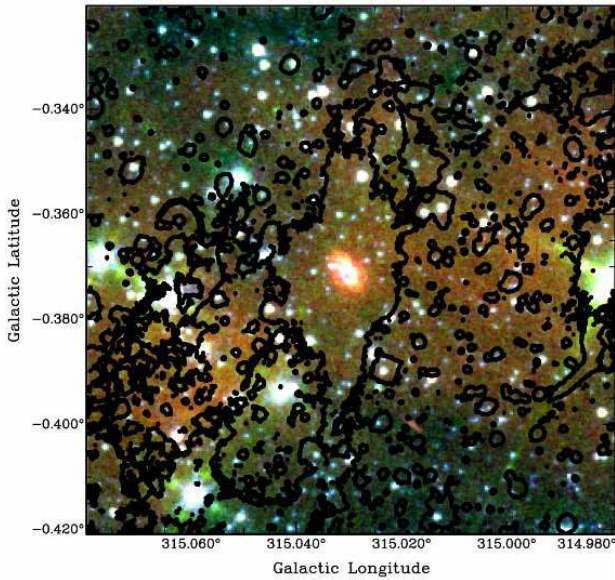


Figure 8. $10'$ by $10'$ field containing the false colour image of PN G315.0-00.3 (Hen 2-111). This PN has an optical geometric diameter of over 10 arcmin. MIR thermal dust emission is likely to cause the white region at the centre of this PN. No other MIR emission appears to be associated with it. Black contours show the extensive $H\alpha$ filaments.

1.9m SAAO telescope. For details see Parker et al. (2006), Miszalski et al. (2008b, 2009a).

6.1 False-colour *Spitzer* imagery

In our enlarged, clean sample of 136 PNe, 60 percent (82/136) stand out against the ISM background in the IRAC images by their MIR false colours, as described in §2.1. 16 percent of our PNe (22/136)

lack the IRAC data needed in all 3 bands required to create a false colour image while 23 percent (31/136) have IRAC data but cannot be separated from the diffuse ISM emission in the MIR. We designate these false colours by O, R, and V to denote the three dominant false colours that we have noted: orange, red, and violet, respectively when we combine the IRAC bands to create color images. By orange we mean a mix of 5.8 and 8.0 μm ; red, dominantly seen at 8.0 μm ; and violet, a mix of 3.6 and 8.0 μm . A “u” in the false colour column of Table 3 signifies that a PN lacks some of the IRAC data required to create the false colour image. Finally, we use an “X” in this column to indicate that, despite having all the requisite IRAC data (i.e. detections at 4.5, 5.8 and 8.0 μm) there is insufficient false colour contrast for a PN to be recognized in the MIR against the local background.

6.2 Measuring the IRAC colours of PNe

Techniques identical to those developed in Paper-I were used to assess the local sky brightness around each PN. We overlaid the IRAC images outside the contours of the $H\alpha$ image to accurately represent the nebular area, and removed nearby GLIMPSE point sources to provide cleaner sky subtraction. This latter method works only when the central region of the PN is not itself pointlike and there is no obvious MIR central star. Otherwise the diffuse photometry of the residual PN image significantly underestimates the nebular flux because the core will have been removed from the image. The sole difference in approach compared with Paper-I was that we integrated the MIR flux over the area of a PN guided by the H-alpha image even when visual inspection failed to identify the object in an IRAC image. The lower bound on nebular MIR flux is set by the outer boundary of the H-alpha PN image. The outer bound is where the PN is no longer detected above the sky background in the MIR.

Estimates of the extended source aperture corrections required to mitigate the effects of scattered light within IRAC on diffuse photometry have changed over the years since the launch of Spitzer. We have updated the diffuse region colours of Paper-I to the latest (Nov.8, 2007) extended source calibration factors for IRAC, documented by Jarrett ² so that all our diffuse photometry is consistent with a common set of current best practices. For some nebulae we were able to compare our MIR magnitudes with measurements of other groups, for example, Hora et al. (2004), Kwok & Zhang (2008), or Phillips & Ramos-Larios (2009). Direct comparisons based on the latest factors were not always possible. Phillips & Ramos-Larios (2009) still used correction factors from Reach et al. (2005), which introduce magnitude offsets of up to 0.1m compared with the usage of current corrections. Kwok & Zhang (2008) make no mention of which aperture corrections they applied to their MIR photometry, potentially leading to differences as large as 0.33 mag (at 8.0 μm), if no corrections were made. There appears to be accord between the various data sets subject to these uncertainties. Those objects whose photometry shows differences that are not attributable to aperture corrections are large nebulae. Here we have integrated over the entire nebula using the overlaid H-alpha image to set the inner edge of the PDR and integrating outwards until the PN is no longer detected above the local MIR sky background. Note that, for PNe of large angular size, others have measured only the MIR bright central region. Hen 2-111 (PN G315.0-00.3) (§5), is a good example. Kwok & Zhang (2008: cited by Hora et al. 2008a)

² <http://spider.ipac.caltech.edu/staff/jarrett/irac/calibration/index.html>

measure an extent only $10\text{--}15''$ for this object in the MIR. The bright nebular core in $H\alpha$ is $29'' \times 15''$ but the PN is seen in deep SHS $H\alpha$ imaging to have a size of order $600''$. The associated MIR emission of the entire nebular is 2 to 3 mag brighter than the bright, dust-dominated core. A less extreme example that indicates that MIR emission in an PN should be sought over at least the area in which $H\alpha$ is apparent is Hen 2-84 (PN G300.4-00.9). The $H\alpha$ size is $36'' \times 24''$ and the IRAC emission corresponding to the $H\alpha$ area is fully 1 mag brighter in all four bands than that measured in the $10''$ region noted by Kwok & Zhang (2008).

The IRAC colours in Table 4 are calculated from the differences between the diffusely calibrated photometric magnitudes for a given PN. If a PN was detected in only one IRAC band then no colours can be derived; e.g. MASH-I PN, PHR1635–4654 was detected only at $5.8\mu\text{m}$. The quantities tabulated for each subset of PNe are the 6 median IRAC colours, each with its standard error of the median (sem), the number of PNe contributing a colour to each median, and the total number of nebulae that belong to each subset. Individual PN IRAC magnitude uncertainties are between 0.02m and 0.15m in bands 1,2 and between 0.07m and 0.23m in bands 3,4. These depend primarily on the local variations of the surface density of stars in IRAC bands 1 and 2, and on sky background variations in bands 3 and 4. These errors include the uncertainties in the IRAC aperture corrections applied to both sky and PN photometry. The resulting errors in our colours could be as little as 0.03 for $[3.6] - [4.5]$ to as large as 0.24 for $[5.8] - [8.0]$.

Table 4 presents 17 different subsets of the PN sample that we have constructed according to various PN properties we are investigating, together with all PNe combined. The colours of our MASH-I and MASH-II nebulae, and of all MASH PNe (MASH-I and MASH-II) are compared with those of previously known nebulae. Other subsets represented are those PNe that appear orange, red, or violet in their IRAC false colours; all PNe contrasted against the ISM having any of these three false colours. These can be compared with the colours of all PNe that are detected in the MIR but are not distinguished from the ISM by visual inspection of the images.

6.3 The IRAC colours of different PN subsets

Comparing MASH-I and MASH-II nebular colours from Table 4 it is clear that five of the six IRAC colour indices are apparently indistinguishable between these two MASH samples. The remaining colour, $[4.5\text{--}5.8]$, differs marginally (3.3σ) between MASH-II PNe and other sets. The sense of this difference is that $[5.8]$ is brighter or that $[4.5]$ is fainter in MASH-II PNe. §6.2.1 shows that our MASH-II PNe sample has a far smaller fraction of bipolar nebulae (13 percent) than both the MASH-I sample (29 percent) and the SEC set (34 percent). Note that this may be an underestimate of the true MASH-II PNe bipolar fraction as there are a higher fraction of compact objects in MASH-II that has made morphological classification difficult. Nevertheless, the typical $[4.5\text{--}5.8]$ colour for the general MASH-II PNe sample is statistically the same as that for all non-bipolar nebulae in our combined sample (they differ by only 1.6σ) so that the bipolar nebulae that are present are not sufficiently numerous to affect this colour balance.

Ybarra & Lada (2009) note that, in dissociative (J-type) shocks that heat gas to above 4000 K, CO is vibrationally excited, as are [FeII] fine structure lines. Both the CO emission lines and most of the [FeII] lines within the overall wavelength range of IRAC fall into the IRAC $4.5\text{--}\mu\text{m}$ bandpass. While we under-

stand the difference between the discovery space for MASH-I and MASH-II PNe, one might wonder whether there are also spectral differences in the dominant MIR emission mechanisms of PNe in these samples. In the NIR, most PNe spectra are dominated by hydrogen recombination lines (Hora et al. 1999, their Table 1) while the next most frequent set of PNe show both hydrogen recombination lines and those of H_2 . These authors list very few nebulae that are dominated by H_2 lines and these tend to be unusual or rare objects, such as edge-on bipolars or proto-planetary nebulae. PNe in the MIR reveal more fine structure lines and strong, broad, dust emission features are common so it is highly likely that most PNe, depending on their evolutionary state, inherent metallicity and morphology, will display a variety of MIR emission processes, rather than being dominated by a single mechanism.

Among the IRAC false colour subsets for the PNe samples we have created we see only two marginally significant (3.0σ) differences. PNe with a predominant orange false colour differ statistically from violet PNe only in the $[3.6\text{--}8.0]$ colour. Because the distinction between orange and red false colours is somewhat subjective, we decided to merge the orange and red looking PNe and compared their combined colours with those of violet PNe, which presents the same difference in $[3.6\text{--}8.0]$. A broader version of this search for colour differences was executed by seeking colour distinctions between the subset of 82 PNe that are visually contrasted against their surroundings and the 31 PNe that reveal no such contrast. Here too there is a single distinction (3.0σ) in that those PNe that stand out against the ISM have a smaller median $[4.5\text{--}5.8]$ colour in the same sense as MASH-II PNe compared with other PN samples (discussed above).

6.3.1 IRAC colours of the general PN population

Stanghellini et al. (2000) found for LMC PNe that morphology is a good indicator of the progenitor population. Therefore we carried out a related test, namely to look for IRAC colour differences between the samples of Type I and non-Type I PNe that we have determined based on our comprehensive optical spectroscopy (see Frew & Parker (2010; their Fig.4). It is already known that there appears to be a strong correlation between a PN being Type I and also having bipolar morphology. However, for these comparisons too, no meaningful colour differences were found. Another aspect of Type I PNe in our sample that is of interest is the proportion of these nebulae to be found in different regions. A volume-limited empirical estimate from PNe within 1 kpc of the sun gives 10 percent (Frew, Parker & Russeil 2006), while Moe & De Marco (2006b) estimated theoretically a value of 6 ± 4 percent, assuming that stars above $4M_{\odot}$ are the progenitors of Type I PNe. We find 25 percent of our clean sample are Type I PNe. Therefore, GLIMPSE confirms that a Galactic latitude-selected sample of PNe is dominated by high-mass stellar progenitors.

The largest morphological group of nebulae is represented by elliptical PNe that constitute 48 percent of the clean sample (65/136). There are only 14 round, 5 irregular, and 4 asymmetric PNe in the clean sample. But the ensembles of round and elliptical PNe also display no colour distinctions. The small group of PNe for which high spatial resolution imagery is lacking are not distinguished from any others by their colours either. Beyond the few distinctions cited above we found no additional significant colour differences in this table between groups of PNe.

6.3.2 Bipolar versus non-bipolar PNe

Of particular interest are the colours of bipolar versus non-bipolar PNe. Therefore, we have separated all bipolar nebulae from non-bipolar nebulae to determine whether this aspect of morphology is reflected in the MIR colours of PNe. In our clean sample of MASH-I nebulae, 29 percent appear bipolar (19/65). For MASH-II PNe the corresponding number is 13 percent (4/31). Of our MASH-I and MASH-II nebulae combined, 24 percent are bipolar (23/95). This rises to 34 percent (15/41) for the SEC objects, probably because these earlier discoveries are brighter nebulae whose morphologies were more readily recognized. Overall the total GLIMPSE-selected clean PN sample contains 27 percent (37/136) bipolar PNe. For comparison we have assembled a non-bipolar subset by excluding all PNe with a “B” descriptor and all those characterized as “S” (i.e. unresolved or point-like nebulae) of which there are 13 instances. Morphologies for these compact objects remain indeterminate. There are thus 87 non-bipolar objects, accounting for 64 percent of the sample.

Bipolar PNe contain dusty disks. Some of these are likely to present an edge-on dusty disk aspect in our direction. In crudest terms this suggests the prospect of a difference in the range of dust temperatures viewed and, therefore, revealed in the MIR. Edge-on dusty disks might appear cooler and redder than PNe lacking either flattened structures or with strongly inclined disks. Based on Gatley’s Rule (§4), which states that only bipolar PNe show strong H_2 emission in the near-infrared, one might have anticipated an analogue for the IRAC 4.5- μm band which encapsulates such features. Somewhat surprisingly, we see no such difference. However, the rule was based on imaging in the 2.122 μm line and the inference is that in the equatorial dusty disks of PNe molecular material ejected by red giant precursors survives and is subsequently shocked by ionized outflows (e.g. Kastner et al. 1996). Ybarra & Lada (2009) have computed the strengths of H_2 lines that arise in low temperature shocks, where H_2 is the dominant coolant, and that fall within the IRAC bands. Whether the emission arises through shocks or by fluorescence one expects all the IRAC bands to contain H_2 lines. Indeed, Hora et al. (2004) and Hora & Latter (1996) have commented on the presence in PNe of the S(9) line at 4.69, the S(7) and S(5) lines at 5.51 and 6.91 μm , and two additional strong lines in the 8.0- μm band. Consequently, the multiple contributions to the IRAC bands from these various H_2 emission lines make it unlikely that H_2 would dominate any specific IRAC colour signature for any PN ensemble. Based on our 136 PNe, there is no unique MIR colour that serves as an indicator of bipolar PNe, like Gatley’s Rule for the presence of H_2 in the NIR. However, Miszalski et al. (2009b) note a tendency for bipolar PNe to be associated with 8.0- μm emission in their waists but no other prominent IRAC emission. The low surface brightness of MASH PNe might militate against IRAC detections of such nebular waists but H_2 might be bright enough to be detected in some PNe. A possible analogue might be RCW69 (Paper-I; Fig.12) which is a large faint PN associated only with weak IRAC emission at 8.0 μm , albeit slightly displaced from the PN waist.

Consequently, one firm result from our study is that there do not appear to be any clear MIR distinctions between the IRAC colours of the overall PNe population, whether segregated by discovery method, MIR false colour, or optical morphology. But PN contaminants do exhibit such distinctions (§6.4). Therefore, the general MIR colours of the combined MASH and previously known PNe sample appear to be highly robust and representative of the PN phenomenon.

6.4 Colour-colour planes

In Paper-I we illustrated that the nominal box occupied by PNe in MIR colours suffered very little contamination by other types of point source, although the disposition of diffuse and compact HII regions in at least one IRAC colour-colour plane might encroach on the predicted location. We have now explored this important issue in some detail as it affects our ability to provide robust loci for true PN in selected colour-colour planes. One problem area is for unresolved or barely resolved PNe which could be contaminated by a wide range of common Galactic point source emitters. We must also explore the isolation of IRAC colours of resolved PNe from the various kinds of possible diffuse contaminants. The IRAC colours are available empirically for diffuse and compact HII regions (Cohen et al. 2007b) while synthetic colours can be estimated for UCHIIIs from spectral libraries such as that inherent in the SKY model of the point source sky (Cohen 1993). Table 5 gives both these colour sets. We then examined the formal metric separations between the median colours of our entire PN sample (Table 4: “All PNe”) and those of diffuse and compact, and UCHIIIs, seeking the statistically most significant colour differences. This analysis yields the optimal MIR colour-colour planes for separating PNe from these common types of interloper.

This approach is justified by calculations of the varying surface density of contaminants throughout the plane at latitude zero in the GLIMPSE region. At 8.0 μm , to IRAC’s local confusion-limited mag, SKY indicates that UCHIIIs contribute from 20 sources deg^{-2} at longitude 10° , 10deg^{-2} at 330° , to 2deg^{-2} at 65° . Diffuse HII regions would be in addition to these point sources.

Table 5 contains two sets of colours for the objects most frequently confused with PNe, namely HII regions. The first line offers the synthesized median colours (in Vega-based magnitudes) of UCHIIIs based on empirical templates for these objects. The synthetic photometry was carried out using the newest relative spectral response curves for the IRAC bands (see Hora et al. 2008b). The second line presents the diffusely calibrated colours of diffuse and compact HII regions (whose colours are indistinguishable). These data were used to plot the corresponding boxes in our colour-colour planes that represent the median locations of these contaminants in the three planes which we discuss below.

Table 5 shows that PNe are well separated from UCHIIIs, their chief contaminants, in $[3.6] - [4.5]$, $[3.6] - [5.8]$ and $[5.8] - [8.0]$ by 5, 5 and 6 σ , respectively, and marginally (3 σ) in $[4.5] - [8.0]$. The metric distances between the median colours of PNe and diffuse HII regions are substantial in all their colours except $[3.6] - [4.5]$, which is just over 3 σ . The differences in $[3.6] - [5.8]$, $[3.6] - [8.0]$, $[4.5] - [5.8]$, $[4.5] - [8.0]$ and $[5.8] - [8.0]$ are 5, 10, 8, 14 and 15 σ , respectively. These conclusions guide the choice of the optimal colour-colour planes for the recognition of PNe.

We attribute these different degrees of colour distinction between the two kinds of HII region and PNe to two aspects of their IR spectra. First, deep 10- μm silicate absorptions characterize UCHIIIs but are absent in diffuse regions where the central star is no longer MIR-bright. Secondly, the ratio of the 6.2- μm PAH band to that at 7.7 μm is greater in HII regions than in PNe (Cohen et al. 1989). These effects reduce all colour indices with respect to the 8.0- μm band in UCHIIIs and enlarge those with respect to the 5.8- μm band in diffuse regions

When performing our MIR characterisation of PNe we prefer to consider PNe bright enough to be detected in all IRAC bands so that all six colour indices are available. We avoid the degenerate planes in which one IRAC band is common to the colour indices

Table 4. Diffusely calibrated median colours (in Vega-based magnitudes) of PNe in the six IRAC indices for different subsets of PNe and for all nebulae combined. Median and standard error of the median (sem) are given together with the number of PNe that contribute to a colour and the total number of PNe available in that sample.

Subset	[3.6] – [4.5] No.	[3.6] – [5.8] No.	[3.6] – [8.0] No.	[4.5] – [5.8] No.	[4.5] – [8.0] No.	[5.8] – [8.0] No.	Sample No.
All PNe	0.81±0.08 107	1.73±0.10 110	3.70±0.11 106	0.86±0.10 115	2.56±0.11 121	1.86±0.07 116	136
MASH-I	0.63±0.15 41	1.88±0.22 42	3.33±0.23 40	1.20±0.17 49	2.69±0.20 55	1.74±0.14 50	65
MASH-II	0.78±0.12 28	1.43±0.10 28	3.19±0.16 28	0.48±0.14 27	2.33±0.13 28	1.88±0.08 28	30
MASH	0.70±0.10 69	1.72±0.14 70	3.22±0.15 68	0.96±0.12 76	2.45±0.14 83	1.81±0.10 78	95
Known	0.92±0.13 38	1.73±0.14 40	3.86±0.15 38	0.83±0.16 39	3.07±0.16 38	2.11±0.09 38	41
Orange	0.72±0.11 26	1.84±0.10 26	3.81±0.14 26	1.07±0.15 27	3.11±0.17 27	1.97±0.09 27	27
Red	0.92±0.09 38	1.49±0.13 38	3.69±0.14 38	0.64±0.13 37	2.45±0.12 38	2.02±0.08 38	38
Violet	0.51±0.14 15	1.30±0.26 15	2.84±0.29 16	0.63±0.40 16	1.86±0.41 17	1.71±0.16 17	17
O+R	0.81±0.09 64	1.71±0.09 64	3.75±0.10 64	0.78±0.10 64	2.69±0.10 65	1.99±0.06 65	65
Contrast	0.81±0.06 79	1.70±0.09 79	3.69±0.10 80	0.74±0.11 80	2.46±0.12 82	1.86±0.06 82	82
No contrast	0.73±0.28 24	1.95±0.31 25	3.81±0.36 24	1.38±0.18 31	3.07±0.28 31	1.86±0.14 31	31
Type I	0.81±0.21 27	1.71±0.24 28	3.21±0.26 28	0.97±0.22 33	2.77±0.28 33	1.68±0.16 32	34
Non-Type I	0.80±0.08 80	1.74±0.11 82	3.75±0.12 78	0.85±0.10 82	2.54±0.10 88	1.91±0.08 84	102
Bipolar	0.98±0.15 28	2.04±0.21 30	3.68±0.22 29	0.97±0.23 31	2.51±0.30 32	1.68±0.19 33	36
Non-Bipolar	0.71±0.11 66	1.52±0.12 67	3.46±0.15 64	0.76±0.11 71	2.46±0.11 76	1.86±0.08 70	87
Elliptical	0.87±0.13 51	1.70±0.16 50	3.75±0.17 49	0.74±0.14 54	2.67±0.13 56	1.92±0.08 53	65
Round	0.68±0.23 11	1.35±0.15 13	3.09±0.22 11	0.86±0.25 13	2.22±0.31 13	1.77±0.24 13	14
Starlike	0.79±0.07 13	1.76±0.24 13	3.87±0.25 13	1.00±0.21 13	3.12±0.23 13	2.05±0.07 13	13

Table 5. Diffusely calibrated median colours (in Vega-based magnitudes) for HII region contaminants, whether ultra-compact, compact or diffuse. Median and standard error of the median(sem) are given.

Subset	[3.6] – [4.5]	[3.6] – [5.8]	[3.6] – [8.0]	[4.5] – [5.8]	[4.5] – [8.0]	[5.8] – [8.0]
UCHII	1.49±0.12	2.50±0.12	3.57±0.12	1.01±0.12	2.08±0.12	1.07±0.12
Diffuse & compact HII	0.47±0.06	3.08±0.10	4.85±0.10	2.60±0.07	4.43±0.05	1.84±0.05

on both axes, which can lead to specious correlations. We offer three different diagrams for IRAC colours: [1-2] vs. [3-4], [1-3] vs. [2-4], and [1-4] vs. [2-3] (Figs. 9, 11, and 12, respectively). Each plot also displays boxes which represent the median distribution of all PNe±3 sem and similar boxes for diffuse HII regions (labeled ‘P’ and ‘H’ in the diagrams), respectively. We also present Fig. 10, showing our entire sample of 136 PNe in the Fig. 9 plane to better present their overall distribution.

Although it is traditional to plot PNe in the [1-2] vs. [3-4] plane (e.g. Hora et al. 2004), one must consider both the distance between UCHIs (the filled circle in all these colour-colour plots) and the PN boxes, and that between diffuse HII regions and the PN boxes. The [1-2] vs. [3-4] plot places the PN box far from the

filled circle that denotes the typical location of bright unresolved HII regions but there is clearly some modest overlap with diffuse HII regions, as expected of these empirically most common contaminants. For well-resolved PNe the [1-3] vs. [2-4] plane separates their colours from those of diffuse HII regions. There is some encroachment by reflection nebulae in this plane although that is easily resolved by visual inspection of H α and Short Red continuum images (a reflection nebula is about as bright in both images). Likewise, for PNe that are not of small apparent size, the [1-4] vs. [2-3] plane most widely separates the relevant objects but, ironically, the right-hand side of the PN box in this plane also includes the location of UCHIs. Each of the three colour-colour planes offers advantages and disadvantages. However, one can readily select

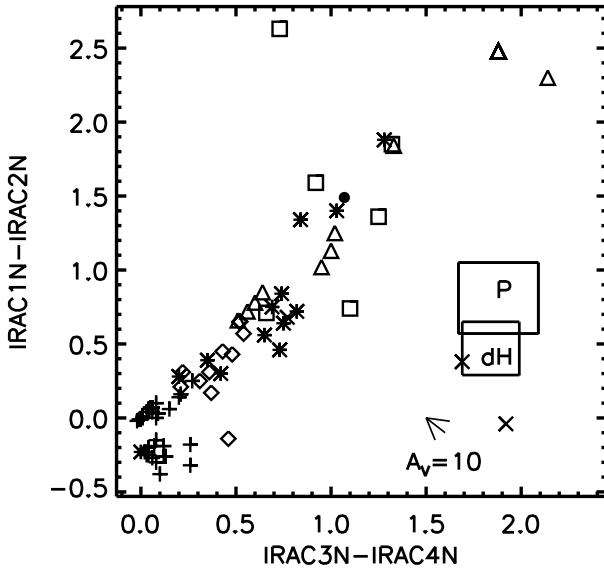


Figure 9. Detail of the IRAC 1–2 vs. 3–4 plane comprising the combined generic locations of 87 different types of IR point source. Key: pluses - normal dwarfs, giants, supergiants; asterisks - AGB M stars; diamonds - AGB visible C stars; triangles - AGB deeply embedded IR C stars; squares - hyperluminous objects (these objects include deeply embedded OH/IR stars and early-type hypergiants (Cohen 1993); a small number are required to reproduce MIR source counts at low latitude: Wainscoat et al. 1992); crosses - exotica (T Tau stars, reflection nebulae); filled circle - UCHIIIs. The reddening vector corresponding to an A_V of 10 mag is shown by the shaft of the arrow in the lower right corner. Two rectangles are also plotted for the median ± 3 sem boxes for diffuse HII regions (labelled “dH”) and for the colours of our entire PN sample ((labelled “P”). The use of the “N” in the IRAC band designations (IRAC1N, etc) signifies the usage of the latest relative spectral response curves for IRAC (Hora et al. 2008b).

a suitable colour-colour plot that would reduce the level of a major contaminant. This is particularly true in the Galactic plane, whether one is working with unresolved or with large PNe. In summary, IRAC MIR colour-colour planes can provide an effective means of separating PNe from their primary contaminants, namely HII regions.

This paper is a proof of concept of a new approach to find PNe using only IRAC colours. To test the method we retain our strong rejection of potential contaminants. In future work we shall hone the technique by balancing colour box extent against rejection of non-PNe.

Those PNe that can be recognized against the local ISM background appear in only three MIR false colours when using the IRAC 4.5, 5.8 and $8.0\mu\text{m}$ bands to encode blue, green, and red, respectively. These are distinct from the false colours of HII regions in this same scheme, offering a useful discriminant. The three false colours in these composite images are the same as were found in Paper-I. Examination of the 82 PNe that reveal false colour above their surroundings shows the following frequencies of PNe by colour: 25 orange (32 percent); 36 red (46 percent); and 17 violet (22 percent). These proportions are very similar to those found for a sample of 47 LMC PNe. These were observed with Spitzer’s IRS (InfraRed Spectrometer) by Stanghellini et al. (2007) and by Bernard-Salas et al. (2009). We find that 42 of these are contrasted against their local ISM. Their false colours appear with similar frequency to those of Galactic PNe. The corresponding proportions for

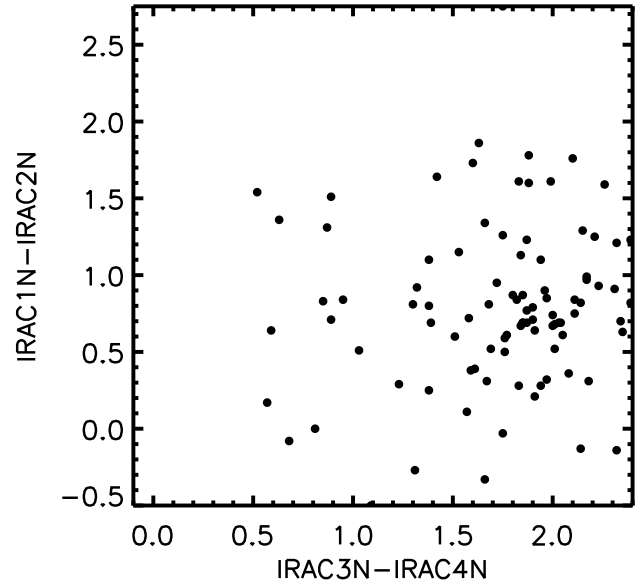


Figure 10. As in Fig. 9 but showing only the distribution of the 136 PNe in this plane.

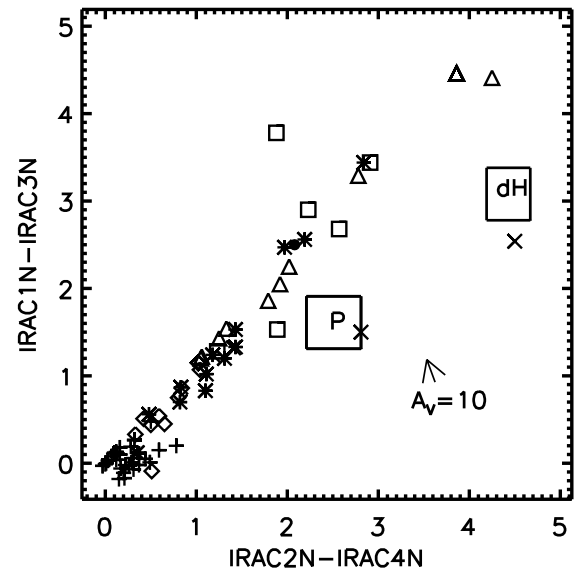


Figure 11. As in Fig. 9 but for the IRAC 1–3 vs. 2–4 plane. .

LMC PNe are 32 percent; 51 percent; and 13 percent. That the same three false colours of PNe occur in the LMC and in our Galaxy, and with rather similar frequencies, suggests that these PN colours arise anywhere from the same mix of physical emission processes.

7 AN OPTICAL EMISSION LINE NEBULAE

DIAGNOSTIC DIAGRAM

SMB proposed a diagnostic plane based on the ratios of common optical nebular emission lines as a means to separate the various kinds of nebular objects according to their excitation mechanisms, physical sizes, and electron densities. For example, Herbig-Haro

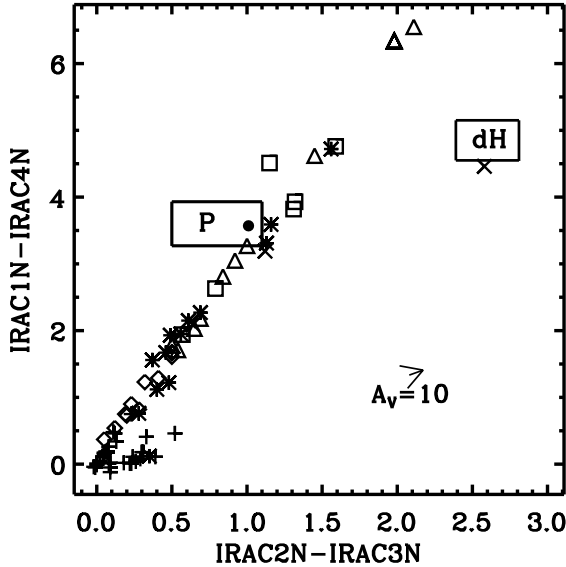


Figure 12. As in Fig. 9 but for the IRAC 1–4 vs. 2–3 plane.

objects and SNRs are shock-excited, while HII regions and PNe are photoionized and distinct domains were identified by SMB to show where SNRs and HII regions lie. The bulk of the area of this plane was occupied by PNe whose range was bounded by two curves, both quasi-linear. Further, PNe of larger physical scale were located to the lower left of the region between the two lines, and smaller PNe to the upper right. The PN region was extended in both directions by dashed lines. A subsequent rendition of the log-log plane of $H\alpha/[SII]$ vs. $H\alpha/[NII]$ became known as the “Canto diagram” (Canto 1981) but we shall cite this diagram as the SMB plot. The original SMB PN domain was empirically enlarged by Riesgo & Lopez (2006) on the basis of a sample of 613 nebulae. The purpose of this extension was to apply this plot to modern PN catalogues that present a much larger range in PN line ratios than was available to SMB. Riesgo & Lopez (2006; their Fig.4) represent the extended range of PNe by an ellipse which accommodates 85 percent of their PN sample. However, this encroaches on almost half the area of the originally designated HII regions’ box. Therefore, we prefer to use the quasi-linear bounds shown by Riesgo & Lopez (2006; their Fig.1). Bipolar PNe are mostly located near the lower bounding line. Corradi et al. (1997; their Fig.3) studied 19 such objects and presented the SMB plot. 58 percent of these PNe fall below the bounding line; the remainder are widely scattered throughout the plane.

In this paper we have used solely our own optical spectra in generating equivalent diagnostic diagrams, preferring to use a homogeneous data set with a uniform reduction process. For our purposes, it is convenient to use the customary SMB diagram to highlight both similarities and differences between groups of PNe. However, a new and far more detailed version of this diagram based on a careful evaluation of about 3000 emission-line objects is being developed by Frew et al. (2010, in prep.) A preliminary version of this plot is presented by Frew & Parker (2010; their Fig.4), incorporating many new MASH PNe. Those authors showed that Type I PNe (following the KB94 definition) inhabit a distinct region in the SMB plot, and are well separated from non-Type I objects. For those GLIMPSE PNe without abundance determinations in the literature, we placed each PN onto our revised SMB plot to determine

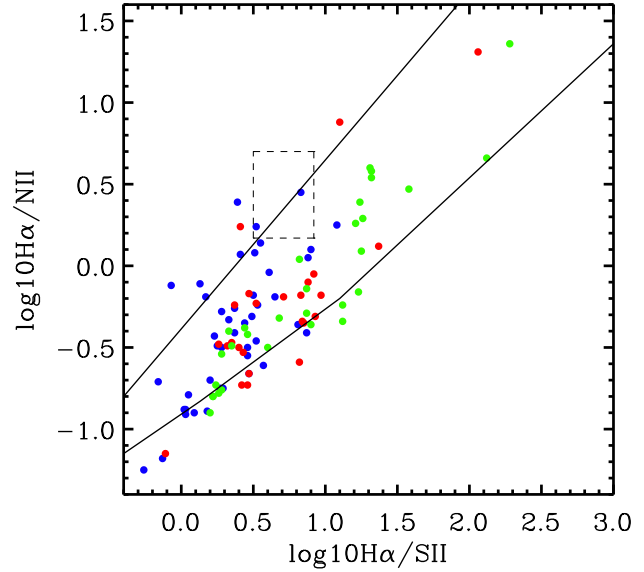


Figure 13. The SMB diagram for all PNe in our sample. Symbols: blue - MASH-I; red - MASH-II; green - previously known PNe. The dashed box is that defined by SMB for HII regions. The two black lines are the bounds to the extended PN zone that accommodates the PN sample of Riesgo & Lopez (2006).

if a nebula was Type I, based solely on the relative de-reddened strengths of the red emission lines in our spectra.

Our three samples of MIR detected PNe appear quite similarly distributed in the SMB plot (Fig. 13). Most lie between the traditional bounding lines or slightly below the lower line. The PNe known prior to MASH are rather more dispersed than MASH nebulae, perhaps reflecting the heterogeneity and lesser accuracy of their line measurements compared with the homogeneous values achieved by MASH follow-up spectroscopy. For example, the two nebulae that lie in the upper right corner of the plane may simply have very weak nitrogen lines, elevating the ratio of $H\alpha$ to $[NII]$. We have omitted the region where SNRs are located but we note that none of our nebulae lie within this zone. A single object (PHR1544-5607) might lie on or close to the SNR boundary ($-0.07, -0.12$). It does have strong $[SII]$ emission lines, is fairly indistinct in the optical imagery and is designated only as a possible PN in MASH. We also indicate the commonly used dashed box that characterizes HII regions. It is of interest that only two PNe are found inside this latter box, PHR1507-5925 and PHR1622-5038, perhaps validating our efforts to eliminate HII regions from the PN sample. The former is regarded as a True PN; the latter has reasonable morphology for a PN, $[OIII]$, and no $H\beta$ in the blue so it is classified as a Likely PN.

Had Mz 3 been plotted in Fig. 13 it would have appeared at (3.08, -0.09), far from all PNe, confirming a further difference between its true character and those of accredited PNe.

Fig. 14 presents the same plane but now colour-coded according to the MIR false colour of PNe that can be distinguished from their surroundings. Red is the most commonly found false IRAC colour for PNe and these are well-distributed throughout the PN zone. By contrast, orange nebulae (with a single exception) are located only from about the centre of the PN zone down to the lower left extreme of the PN zone. Violet false-coloured PNe are more widely dispersed than orange PNe, despite their relative paucity. This suggests that orange PNe are more evolved than other PNe.

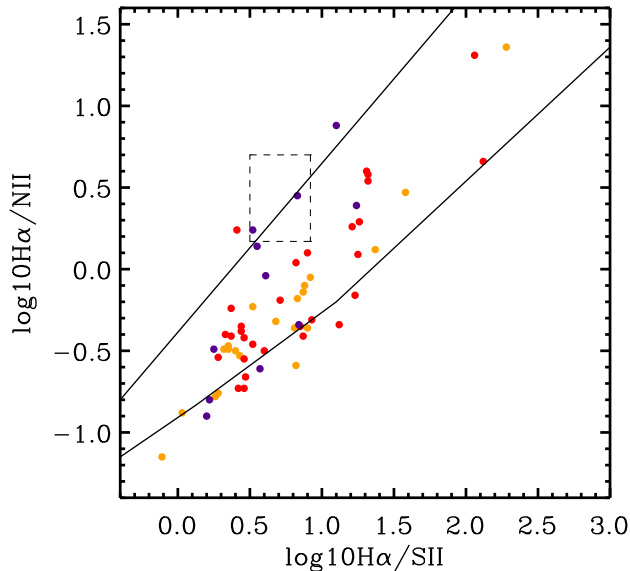


Figure 14. The SMB diagram for all PNe in our sample as for Fig. 13. Symbols are colour-coded to match the red, orange, or violet MIR false colours of PNe.

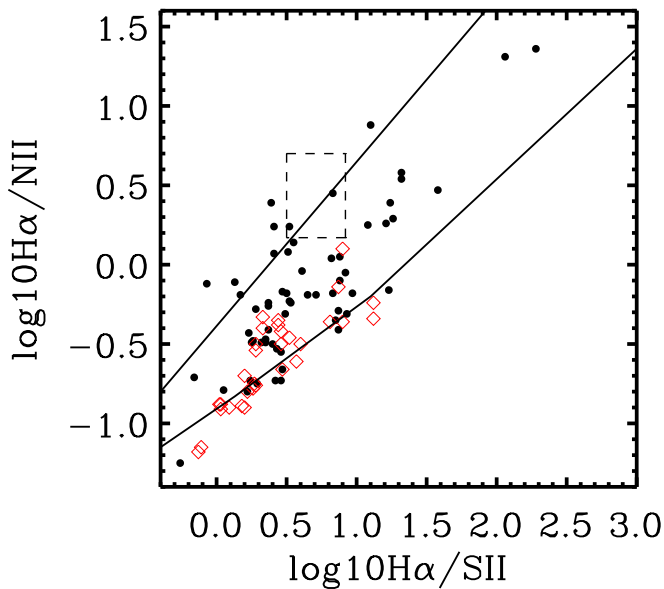


Figure 15. The SMB diagram for all PNe in our sample as for Fig. 13 but distinguishing bipolar from non-bipolar nebulae. Symbols: black - non-bipolar PNe; red - bipolar PNe.

All three false colour samples appear to be equally likely to contain bipolar nebulae, based on their distribution near and below the lower bounding line.

Our third variation on the SMB plot (Fig. 15) distinguishes between bipolar (open red squares) and non-bipolar (filled black circles) PNe. The distribution of bipolar PNe in our sample is much more restricted than that of the smaller Corradi et al. (1997) sample. We find that bipolar nebulae occur only to the left of the centre of the PN zone. The area of the entire PN zone that contains bipolar PN is less than one third of the total area of the PN zone. If our clean PN sample pertains to all PNe then this is a substantial reduction in

Table 6. Median radii in pc for PNe as a function of age for each group. The median and standard error of the median (sem) are given.

Subset	No. of PNe	median radius	sem
Known	38	0.12	0.04
MASH-I	63	0.34	0.04
MASH-II	31	0.15	0.03
All MASH	94	0.25	0.03

the area of the SMB diagnostic plot in which one might expect to identify PNe as bipolar. Using our cleaned sample of PNe suggests that the diagnostic value of the SMB plane for bipolar PNe might be sharper than previously thought, perhaps due to the careful morphological classification of the MASH sample in particular, even when based on the same imaging data.

8 PHYSICAL RADII OF PNE

We have derived intrinsic sizes (radii in parsecs) for most of the PNe in our overall sample based on the calculated $H\alpha$ SB-distance relation (Frew, 2008; Frew & Parker 2010), using the observed angular dimensions, a measured $H\alpha$ flux and a reddening. Literature distances, if available and deemed sufficiently reliable, are also used where necessary. Many of the $H\alpha$ fluxes and reddenings, (which will appear in a separate publication), although evaluated as carefully as current data will allow, are preliminary, so that the distances (and hence radii) should currently be taken with some caution. A few of the reddenings were determined from unpublished MASH line fluxes, and others from a comparison of $H\alpha$ and radio fluxes. To do this, we assumed that the 6-cm flux is the same as the flux density given in this paper.

However, we hope that some statistical conclusions might emerge from the ensemble of sizes when we employ PN radii as proxies for PN age.

We have chosen to assign our PN sample to a few selected size bins for the present, although further efforts (Frew 2010, in prep.) will offer both new and improved determinations and refinements of the reddenings, fluxes, and sizes. The adopted colour code to represent the bins is as follows: turquoise, very young PNe, radius <0.1 pc; blue, young, radius $0.1-0.2$ pc; green, middle-aged, $0.2-0.4$ pc; orange; old PNe, $0.4-0.9$ pc; and red, senile PNe, >0.9 pc. We adopt a radius of 0.9 pc rather than 0.8 pc to be consistent with the completeness radius of Moe & De Marco (2006b). Despite the input data being preliminary, we find clear trends in the SMB diagrams with PNe evolving from upper right to lower left. Table 6 indicates median PN radii for different groups of PNe.

Consequently, the median radius of PNe increases from the previously known sample, through MASH-II to MASH-I PNe, consistent with the population of MASH PNe generally representing objects that are more evolved (and hence more extended at a given distance) than those discovered pre-MASH (Parker et al. 2006). This is in good agreement, for example, with the work of Tajitsu et al. (1999), whose photoionization models show increasing temperatures towards the lower left of the SMB plane.

8.1 Relationship between IRAC colours and nebular age

Table 7 investigates whether PNe also change their IRAC colours as they age. The sample of senile PNe is too small to provide meaning-

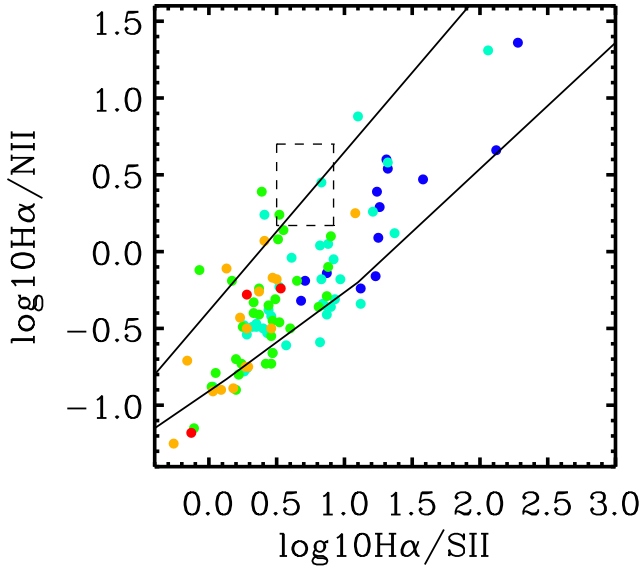


Figure 16. The SMB diagram for all PNe in our sample for which we have assessed the distance and PN physical radius. Symbols: turquoise, very young; blue, young; green, middle-aged; orange, old; red, senile.

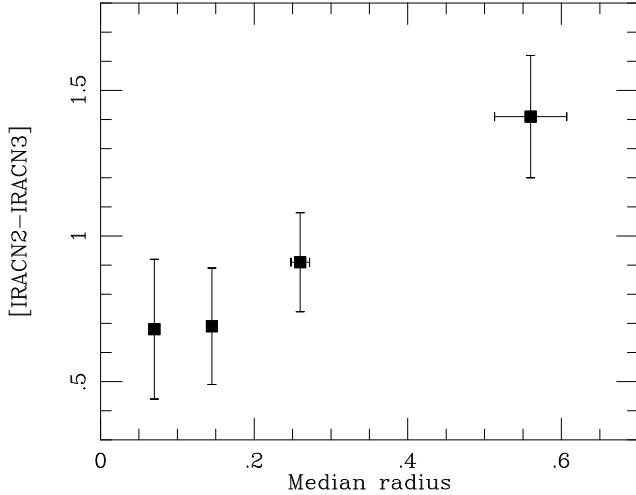


Figure 17. The trend of IRAC [4.5–5.8] colour index with PN age using median sample radius (in pc) as a proxy for each age bin. The index increases from very young to senile PNe.

ful median colours and was, therefore, merged with the old nebulae. Fig. 17 and 18 show clear trends in both [4.5–5.8] and [5.8–8.0] colours as a function of PN age. Both plots can be understood in terms of an increasing contribution from the 6.2- μ m PAH band to the 5.8- μ m flux as PNe and their PDRs expand with time. Recall (§6.3) that MASH-II PNe have marginally smaller [4.5–5.8] than MASH-I PNe. This now solidifies the impression that MASH-II PNe are truly younger and more compact than those found in MASH-I. In Fig. 18, both relevant IRAC bands contain PAH emission suggesting that the relative brightnesses of these two bands change as PNe age. Such an evolution implies that the PN false colours vary with age. The same interpretation applies equally to PNe in which the dominant emission mechanism is by H_2 lines, and

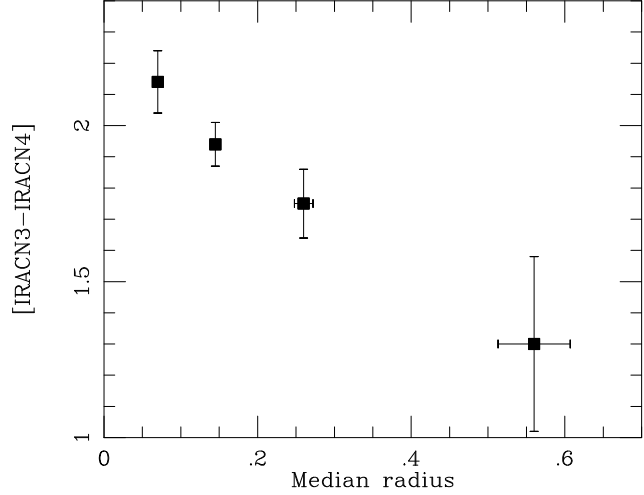


Figure 18. The trend of IRAC [5.8–8.0] colour index with PN age using median sample radius (in pc) as a proxy for each age bin. This index decreases from very young to senile.

requires that the brightnesses of the strongest lines such as those at 4.694, 5.510, and 6.907 μ m evolve accordingly.

Hot dusty haloes have been measured around some PNe (e.g., Phillips & Ramos-Larios (2005)), with dust temperatures in the range 700 to 1200K based on 2MASS colours. This could influence the IRAC photometry at 3.6 microns. There is no supporting evidence to date to show that stochastic heating of very tiny grains produces emission in the IRAC 8.0 and 5.6 micron bands, which would require temperatures between 360K and 520K, respectively.

9 THE RADIO FLUXES OF THE PN SAMPLE

Radio flux densities of the PNe were obtained from the MGPS-2 (Green 2002, Murphy et al. 2007) and NVSS (Condon et al. 1998) surveys, together with data from Condon & Kaplan (1998) and Luo, Condon & Yin (1998). MGPS-2 covers the sky south of -30° Dec. at 843 MHz and NVSS covers the sky north of -40° Dec. at 1.4 GHz. The surveys are comparable in resolution and sensitivity, and together they provide complete coverage of the Galactic Plane at ~ 1 GHz. As in Paper-I, we treat both surveys as if they offered data at a common frequency. Both MGPS2 and NVSS provide on-line access to point source catalogues. For PNe that were not listed in these catalogues we nevertheless inspected the survey images directly. If a credible, though weak, source, was apparent at the PN position, we measured its flux using the MIRIAD task IMFIT to determine the integrated emission above the local background.

In Paper-I we concluded that PNe drawn from the sample consisting only of MASH nebulae were likely to be optically thin near 1 GHz. Bojicic (2010) undertook a radio survey of PNe that are mostly MASH nebulae, previously undetected in NVSS and MGPS-2. On the basis of the PN radio brightness temperatures, these objects would also be expected to be optically thin ~ 1 GHz (Bojicic et al. (2010)). However, 30 percent of the sample of PNe in the present paper consists of compact, high-surface brightness PNe, known prior to MASH, many of them young. One expects these PNe to be optically thick at low frequencies (e.g. Pazderska et al. (2009; their fig.7)).

Table 7. IRAC colour indices for subsets of PNe according to age. Median and standard error of the median (sem) are given together with the number of PNe that contribute to a colour and the total number of PNe available in that sample.

Subset	[3.6] – [4.5] No.	[3.6] – [5.8] No.	[3.6] – [8.0] No.	[4.5] – [5.8] No.	[4.5] – [8.0] No.	[5.8] – [8.0] No.	Sample No.
Very Young	0.84±0.13 17	1.63±0.16 18	3.87±0.17 17	0.68±0.24 17	2.96±0.24 17	2.14±0.10 17	18
Young	0.90±0.11 37	1.70±0.17 39	3.59±0.16 38	0.69±0.20 38	2.44±0.19 41	1.94±0.07 39	44
Middle-aged	0.64±0.18 32 31	1.53±0.26 30	3.52±0.27 33	0.91±0.17 35	2.69±0.16 33	1.75±0.11	55
Old+senile	0.60±0.26 16	1.81±0.26 16	2.84±0.33 22	1.41±0.21 23	2.44±0.33 22	1.30±0.28	29

Overall we found that 52 percent (70/136) of our 136 PNe were detected around 1 GHz. As expected, the detection rate is highest for those PNe discovered before MASH: 85 percent (35/41). For the generally more compact MASH-II nebulae the rate is 47 percent (14/30) whereas for MASH-I it is 32 percent (21/65), consistent with a population of evolved PNe having larger diameters and weaker radio emission than previously known nebulae.

From our optical spectra we have examined N_e measured from the ratio of the red [SII] lines to test whether the highest density PNe are those with high MIR/radio simply by virtue of their radio optical depth ~ 1 GHz. We found no correlation, perhaps because these lines cannot probe the highest density regions of PNe whose free-free emission dominates that from the more tenuous nebular regions.

9.1 The MIR/radio flux ratio

In Paper-I we interpreted differences found between the MIR/radio flux ratio for MASH-I PNe (~ 5) and that for a set of 21 SEC PNe, (12), analyzed by Cohen & Green (2001) as indicative of a progressive change in the ratio from previously known PNe to the more highly evolved MASH nebulae. However, we have re-examined those 21 PNe and found that the MIR fluxes measured by MSX for a significant fraction of these objects were contaminated by other sources due to the location of the nebulae in dense star fields at low latitudes. These caused overestimates in the MIR/radio ratios. This is rarely a problem for the measurement of bright sources, such as HII regions, but accurate photometry with MSX of the faint sources that typify PNe requires caution in the Galactic plane. Therefore, we will not make use of the Cohen & Green MSX fluxes for objects affected by the crowding of the PN fields. Thirteen of these 21 nebulae are included in our new sample of SEC PNe but now all are represented by IRAC images at high spatial resolution, eliminating the difficulties encountered by MSX photometry. The value for this ratio is now a more modest 8.4 for the SEC PNe.

The second column of Table 8 presents our analyses of this ratio for PNe drawn from the different discovery surveys, and by selecting PNe with specific attributes such as the presence or absence of bipolarity in the nebular morphologies. Bright PNe discovered prior to the MASH and lying within the GLIMPSE region contain a high fraction of bipolar nebulae. A bipolar PN viewed close to its edge-on disk plane tends to be brighter in the MIR than a non-bipolar object or a bipolar nebula viewed with its dusty disk face-on. If a PN with a dust disk is seen face-on, the hot dust in the inner part of the disk closest to the star emits brightly in the NIR. For an edge-on **optically thick** disk the observer cannot see

the inner disk directly. The radiation is degraded to the IR and transferred through the disk to the cool outer edge, which is bright in the MIR because it subtends a larger angle than the hot dust and it peaks at longer wavelengths.

One might interpret the large median MIR/radio value of 8.4 for the 33 SEC PNe as consistent with this picture, but the difference between this value and the MIR/radio ratio for all MASH nebulae (3.6) is statistically insignificant given the uncertainties. The same situation prevails for the difference between all our bipolar and non-bipolar nebulae (Table 8). The highest value for MIR/radio (13) is found for the six PNe that lack any contrast relative to their ISM environment but this sample is too small to provide a reliable median ratio. For the ensemble of IRAC colours, the MIR/radio flux ratio for our sample of PNe is also robustly represented by the median value of 4.7 ± 1.1 for the whole sample, virtually identical with the result derived in Paper-I for a much smaller group of PNe (4.6 ± 1.2). This ratio can also serve as a valuable and reliable new discriminant between PNe and HII regions. Diffuse and compact HII regions present large MIR/radio ratios of ~ 25 while UCHIIs have even higher ratios with MIR/radio typically ~ 42) (§2.1.2) The significance of these differences between PNe and UCHIIs is 5σ , and between PNe and compact and diffuse regions it is 4σ .

9.2 The dependence of MIR/radio flux ratio on PN age

It is of interest to probe whether changes in the MIR/radio ratio can be discerned as an effect of PN aging. These ratios are found at the bottom of the second column of Table 8. There appear to be no significant differences between the ratios for very young, young, and middle-aged PNe. Only the sample of old PNe seems distinct, but only three nebulae contribute to the median ratio, and only two of these, PHR1437-5949 and PHR 1843-0232, have high ratios of 20 and 21, respectively. Both are PNe of large angular size, over 1 arcmin in diameter, as expected for old nebulae. It is also possible that the 700 mJy flux density of the latter, detected at $8.0 \mu\text{m}$ in its direction, is contaminated by ISM emission.

That so few PNe are detected in the radio regime among these 29 old and senile objects suggests that most old PNe lose their radio emission faster than their PDRs are destroyed. This is consistent with their great faintness even in H α .

10 FALSE COLOUR AND EXCITATION CLASS

The third column of Table 8 explores the suggestion made in Paper-I that MIR false colours might serve as a proxy for optical excita-

Table 8. Median relationships between nebular excitation assessed as $[\text{NII}]/\text{H}\alpha$ and false IRAC colour for subsets of PNe with different attributes. For each quantity, median and standard error of the median (sem) are given.

Subset	$8.0\mu\text{m}/\text{radio}$ PNe contributing/total	$[\text{NII}]/\text{H}\alpha$ PNe contributing/total
All PNe	4.7 ± 1.1 66/136	2.1 ± 0.3 117/136
MASH-I	3.6 ± 1.0 19/65	2.4 ± 0.4 56/65
MASH-II	3.9 ± 0.8 14/30	2.0 ± 0.5 29/30
MASH	3.6 ± 0.9 33/95	2.2 ± 0.3 85/95
Pre-mash	8.4 ± 2.8 33/41	1.6 ± 0.4 32/41
Orange	10 ± 2.5 21/27	2.3 ± 0.5 24/27
Red	3.3 ± 0.6 30/38	2.1 ± 0.3 34/38
Violet	3.6 ± 1.6 5/17	0.7 ± 0.2 15/17
O+R	4.4 ± 1.0 51/65	2.2 ± 0.3 58/65
Contrast	4.3 ± 1.0 56/78	2.1 ± 0.8 73/78
No contrast	13 ± 3 6/31	3.1 ± 0.7 27/31
Type I	10.5 ± 2.4 14/34	5.4 ± 0.7 33/34
Non-Type I	4.3 ± 1.0 52/102	1.5 ± 0.2 84/102
BPNe	7.4 ± 2.4 21/36	3.3 ± 0.4 34/34
Non-BPNe	3.6 ± 1.0 35/87	1.5 ± 0.3 74/87
Elliptical	3.6 ± 1.0 29/65	1.5 ± 0.5 56/65
Round	4.0 ± 0.8 4/14	1.7 ± 0.2 11/14
Very young	6.0 ± 2 16/18	0.4 ± 0.2 15/18
Young	3.6 ± 1.2 29/44	2.2 ± 0.3 40/44
Middle-aged	6 ± 3 14/41	2.5 ± 0.5 37/41
Old	20 ± 5 3/25	3 ± 0.8 22/25
Old+senile		3.0 ± 1.5 25/29

tion of a PN, and hence also as a crude proxy for central star temperature, expressed as the ratio of $[\text{NII}]/\text{H}\alpha$ line strengths. With our significantly enlarged sample of nebulae we see no progression of the median excitation from orange to red to violet. However, the sole significant difference in this regard, between any pair of PN subgroups, is that between the combined orange+red sample and the violet false colour group. The formal difference is 4.2σ . Optical excitation class, represented by the ratio of $[\text{NII}]/\text{H}\alpha$, is related to false colour in the sense that the combined orange and red PNe are distinct from violet PNe, in the IRAC false-colour representation that we have adopted.

Although violet PNe constituted almost half the sample in

Paper-I, they are now less than 13 percent of our clean combined sample. The dominance of the red and orange PNe suggests that these possibly represent the two most commonly found emission mechanisms in the IRAC wavelength range, namely PAH bands (red) or H_2 lines (orange). The rarer violet PNe must represent a different population of nebulae. In Paper-I we suggested the possibility that violet nebulae might represent two different PN types: objects dominated by H recombination lines, and nebulae of high excitation where the interplay of emission lines in each band caused the violet appearance. We had in mind the possibility of optically very low-excitation spectra for the former and very high excitation for the latter. Note that some PNe in which only the $\text{H}\alpha$ line is seen

in the red without the common lines of [NII], [SII], are found to be very high excitation PNe in which He lines are prominent. It is, therefore, of interest that so few of the violet PNe have radio detections (less than one third: see Table 8, col(2)) perhaps reinforcing the possibility of a distinction based on the degree of ionization. There are 3 radio detections in the low-excitation group (low ratios of [NII]/H α), and only one in the high-excitation group of violet PNe. These numbers are so small that this cannot be regarded as a trend. The potential dichotomy of excitations suggested the importance of re-examining the violet objects.

The 17 violet PNe break down into three groups: 7 with [NII]/H α ratios > 1 ; 8 with [NII]/H α ratios < 1 ; and two PNe for which we lack the requisite spectra. The 7 high-excitation objects have a median ratio of 0.4 ± 0.1 , and the 8 low-excitation nebulae a median ratio of 4.1 ± 1.0 . Further, violet PNe showing only H α in emission are nebulae of small diameter (≤ 20 arcsec), and tend to be elliptical. Most of those with strong nitrogen lines tend to be bipolar. Apparently, false colour violet PNe come from two very different PN categories. This is consistent with the unusually high error found in Table 4 for the median value of [4.5]-[8.0] for false colour violet nebulae: 1.86 ± 0.41 . This is the largest error associated with any colour in this table and could also signify that two very different data sets are merged.

There is an additional clue from the Spitzer IRS spectra of LMC PNe (Stanghellini et al. 2007). Six PNe from the roughly 50 that have IRS spectra have IRAC false colour images that are violet. All of these objects (SMP LMC numbers 10, 28, 35, 45, 72, and 80) are characterized by “featureless” MIR spectra, rising slowly to the red, and lacking any distinct emission peaks of either C-rich or O-rich mineralogy. Despite this uniformity, these PNe span the range from intermediate to very high excitation MIR spectra. We have examined the optical spectra of these nebulae that were obtained by Reid & Parker (2006) and all 6 of these LMC PNe show only H lines. [NII] is completely absent. Many PNe have negligible [NII], [OII] and [SII] lines. These are very high excitation, optically thin PNe, and represent the most evolved PNe in any sample (Richer et al. 2008). It is possible that at least some of these violet PNe are in fact of such high excitation that one ought to acquire blue spectra and seek HeII lines to assess their excitation because the [NII]/H α ratio has definite limitations. Reid & Parker (2010) have revisited the three common methods for the excitation class parameter for a large sample of LMC PNe. They propose an improved scheme which also uses the HeII lines. Most MASH PNe are too faint for meaningful blue spectra to be obtained and we wanted to analyze all nebulae on a uniform basis, limiting the current effort to the use of [NII]/H α .

By contrast, comparing the median excitation classes of Type I and non-Type I PNe indicates a substantial difference (16σ) in the sense expected: Type I nebulae have much higher excitation than non-Type I nebulae, reflecting their more massive progenitors with the associated higher nebular ionization and excitation.

11 COLOUR COMPARISONS WITH THE LMC PNE

We have compared the six IRAC median colours of our 136 PNe in GLIMPSE with those of 588 LMC PNe. We first examined the Leisy et al. (1997) LMC sample of PNe (IRAC data from Hora et al. (2008a), which are the LMC equivalents of the bright SEC sample of early discoveries in the Galaxy (our “previously known” sample). Then we analyzed (Cohen et al. 2010, in prep.) the combina-

tion of the Leisy PNe and the many fainter PNe discovered by Reid & Parker (2006: RP) using IRAC measurements from the SAGE final data release (DR3, 2009-09-22). These source catalogues are based on mosaic photometry and are about 1 magnitude deeper than previous SAGE releases (Sewilo et al. 2009). Table 9 compares our Galactic PN colours with those of the Leisy PNe and with the combined dataset of Leisy and RP PNe which best represents the LMC ensemble of nebulae.

Phillips & Ramos-Larios (2009) tabulated IRAC data for a partial sampling of the RP nebulae. Unfortunately they provide neither average nor median colours. They state that LMC [4.5]-[5.8] indices are significantly higher than for Galactic PNe while [5.8]-[8.0] indices are significantly lower. We disagree with both of these statements. We find no statistically meaningful difference between the median IRAC colours of the 136 Galactic PNe and those of the sample of Leisy LMC PNe and only one meaningful difference between Galactic colours and those of the joint sample of all published LMC PNe. In particular, the colour differences between median Galactic and median LMC PNe in [4.5]-[5.8] and [5.8]-[8.0] are only 0.6 sigma and 2.9 sigma, respectively. The sole significant difference occurs for [3.6]-[4.5], which is much smaller (5 sigma away) for the Leisy+RP PNe than in the Galaxy. However, this is attributable to contamination of the PN photometry by Galactic and Magellanic field stars and even by the central stars of LMC PNe. This phenomenon was noted by Hora et al. (2008a) who refer to these as “objects near zero colour”. If we eliminate all LMC PNe whose [3.6]-[4.5] index is below 0.2, the remaining 333 nebulae have a median [3.6]-[4.5] of 0.76 ± 0.02 , indistinguishable from the same colour indices for Galactic and Leisy PNe. This reinforces the idea that the interlopers are field stars. Despite the consequences for stellar evolution embodied in the very different metallicities of the Galactic and LMC nebulae, no statistically meaningful colour differences are manifest. It is not yet possible to probe more deeply into the corresponding MIR/radio ratio for LMC PNe, because of the current paucity of radio continuum detections (Filipovic et al. 2009).

12 CONCLUSIONS

We have explored the contributions to a multi-wavelength analysis of PNe offered by: the ratios of their red optical lines of H α , [NII] and [SII]; electron densities derived from the [SII] doublet; IRAC false colours; excitation class, defined from the ratio of the [NII]/H α lines; direct overlays of MIR image contours on H α images; and the MIR/radio ratio. To place our goals in context with other efforts, we intend to pursue the possibility of finding new PNe using Spitzer’s IRAC wavelengths (3–8 μ m). However, both Wachter et al. (2010) and Mizuno et al. (2010) have recently described large numbers (over 200 and 362, respectively) of well-resolved bubbles found by visual inspection of Spitzer MIPS 24- μ m images from the MIPS GAL project (Carey et al. 2009). Wachter et al. emphasize symmetric shells with defined peripheries and central sources. These criteria lead to shells associated with Pop-I Wolf-Rayet stars and LBVs. Mizuno et al. do not demand a central source and include filamentary, bipolar, and irregular objects. Their identifications are largely with PNe. Most of these bubbles are detected only at 24 μ m and have no extended IRAC counterparts. It will be of great interest to see whether our IRAC approach will complement the 24- μ m objects or overlap the MIPS

Table 9. Comparison of median IRAC colours (in Vega-based magnitudes) for all our PNe within GLIMPSE-I with colours of LMC PNe from the Leisy et al. (1997) tabulation, as measured in IRAC by Hora et al. (2008a), and 588 Leisy and RP PNe (IRAC from the SAGE project data release of 2009). Median and standard error of the median (sem) are given together with the number of PNe that contribute to a colour.

Subset	[3.6] – [4.5] No.	[3.6] – [5.8] No.	[3.6] – [8.0] No.	[4.5] – [5.8] No.	[4.5] – [8.0] No.	[5.8] – [8.0] No.
GLIMPSE-I	0.81±0.08	1.73±0.10	3.70±0.11	0.86±0.10	2.56±0.11	1.86±0.07
	107	110	106	115	121	116
Leisy	0.76±0.03	1.83±0.06	3.39±0.07	0.92±0.05	2.62±0.07	1.69±0.04
	174	124	141	126	145	119
Leisy+RP	0.58±0.02	1.828±0.05	3.327±0.08	0.928±0.04	2.464±0.06	1.57±0.07
	433	253	254	265	266	217

detections. But our new criteria will certainly help to select the best candidates for NIR/MIR confirmatory spectroscopy.

In summary we are able to make the following points based on our investigations.

- We have shown that 45 percent of the “known” pre-MASH PNe in the GLIMPSE-I region are likely contaminants. From repeated culls of MASH PNe we also estimate that our remaining degree of contamination by non-PNe is 5 percent, almost an order of magnitude lower than that for heterogeneously catalogued PNe found prior to MASH in the same area. We believe that we have assembled a pure sample of 136 PNe to support these multi-wavelength studies that are, therefore, unaffected by any biases that these contaminants would introduce.

- The total MIR extent of a PN should be treated as being at least as large as the entire region emitting in $H\alpha$ even if there is a bright MIR core close to the central star. It is essential to measure a PN’s entire MIR extent by going beyond the tracer of the ionized gas, whether thermal radio continuum or $H\alpha$, because the total MIR emission of a large PN, and its colours, are quite different from the colours of the core.

- The MIR/radio flux ratio and IRAC colour indices of Galactic PNe appear to be robust attributes, invariant among the many groups of PNe into which we have divided our sample. Somewhat surprisingly the colour indices of LMC PNe are statistically the same as those of Galactic PNe implying that any metallicity differences are not reflected in MIR PN attributes, or that these effects contribute less than 0.10 mag to any index.

- Gatley’s Rule appears to have no colour analogue in the MIR. We believe this is because the IRAC bands all contain H_2 lines.

- We find 25 percent of our clean sample are Type I PNe, significantly greater than a volume-limited estimate of 10 percent (Frew, Parker & Russeil 2006). Therefore, GLIMPSE confirms that a Galactic latitude-selected sample of PNe is dominated by higher-mass stellar progenitors.

- Our comparisons show that PN MIR characteristics do not appear to vary with morphological subset, with few exceptions. PN IRAC colours cannot distinguish between bipolar and non-bipolar nebulae. However, Type I nebulae are strongly differentiated by their colours from non-Type I PNe. PN optical excitation class does not correlate with IRAC colour indices either but MIR false colour may be indicative, with a bimodal distribution of violet nebulae including both the lowest and the highest excitations.

- We have presented IRAC colour-colour planes for PNe that are designed to offer the largest metric distances between PNe and HII regions, whether unresolved, diffuse or compact, and to minimize many other point source contaminants.

- We have reduced by a factor of about three the diagnostic area in the SMB diagram in which bipolar PNe are located.

- We have assigned physical radii to all 136 PNe and have used these as proxies for PN age. On this basis we see a real trend between [5.8]–[8.0] colour index and evolution which might itself serve as a more convenient practical determinant of evolutionary stage, at least capable of placing individual PNe in groups like “young”, “middle-aged”, etc.

- The median MIR/radio ratio for all PNe is 4.7 ± 1.1 and it does not vary with PN evolutionary phase making PNe separable from their major contaminant, HII regions, whether compact, diffuse, or ultra-compact.

- From our enlarged sample we have determined that the MIR/radio ratio is not a proxy for PN excitation class, nor is PN false colour.

- We provide a table of 25 rejected objects in the GLIMPSE-I area that are not PNe in hopes that these will no longer confuse other researchers.

- The three clear IRAC false colour guises of PNe must indicate the mix of emission mechanisms that contribute to the IRAC appearance. Regardless of the precise origin of these three colours, we argue that, if a nebula displays any false colour other than these, this alone is sufficient reason to suspect that the nebula might not be a PN as such objects have invariably turned out to be contaminants when morphological, spectroscopic, NIR and other diagnostic criteria are examined.

- PNe are known to suffer dimmings and brightenings and even to undergo outbursts (Shaw et al. 2007; Shaw, Rest & Damke 2009). Therefore, we prefer to use contemporaneous photometry to define the colours that characterize PNe rather than to mingle IR data from several widely separated epochs.

- We used the six IRAC colours from Table 4, defined by the entire sample of PNE, to examine the same median \pm 3sems boxes as shown in our colour-colour planes. We then sought point sources in the GLIMPSE-I catalog that satisfied the six constraints. This query recovered known PNe and returned a significant number of PN candidates. These will be the subject of a future paper (Cohen et al. 2010, in prep.).

13 ACKNOWLEDGMENTS

MC thanks NASA for supporting this work under ADP grants NNG04GD43G and NNX08AJ29G with UC Berkeley. MC is also grateful for support from the Distinguished Visitor program at the Australia Telescope National Facility in Marsfield. TM acknowledges the support of an ARC Australian Postdoctoral Fellowship (DP0665973). The MOST is owned and operated by the University of Sydney, with support from the Australian Research Council and Science Foundation within the School of Physics. The National

Radio Astronomy Observatory is a facility of the National Science Foundation operated under cooperative agreement by Associated Universities, Inc. This research made use of Montage, funded by the National Aeronautics and Space Administration's Earth Science Technology Office, Computational Technologies Project, under Cooperative Agreement Number NCC5-626 between NASA and the California Institute of Technology. This research made use of SAOImage DS9, developed by Smithsonian Astrophysical Observatory.

REFERENCES

- Acker A., Marcout J., & Ochsenbein F., 1996, First supplement to the Strasbourg-ESO Catalogue of Galactic Planetary Nebulae, Observatoire de Strasbourg
- Acker A., Marcout, J., Ochsenbein, F., Stenholm, B., Tylenda, R. 1992, "Strasbourg - ESO catalogue of galactic planetary nebulae" (ESO, Garching)
- Balick, B., 2008, <http://www.astro.washington.edu/users/balick/PNIC/>
- Balick, B., 2009, Proc. APN-IV, pg.19, eds. Romano L.M. Corradi, Arturo Manchado and Noam Soker, I.A.C. electronic publication, p.19
- Becker S.A., & Iben I., 1980, ApJ, 237, 11
- Beer, S.H. & Vaughan, A.E. 1999, PASA, 16, 134
- Benjamin, R.A. et al. 2003, PASP, 115, 953
- Bensby, T. & Feltzing, S. 2006, MNRAS, 367, 1181
- Bernard-Salas, J. et al., 2009, ApJ, 699, 1541
- Boumis, P., Paleologou, E. V., Mavromatakis, F., Papamastorakis, J. 2003, MNRAS, 339, 735
- Bojicic, I., 2010 PhD Dissertation, Macquarie University, Australia
- Bojicic, I. et al. 2010, submitted
- Boumis, P., Akras, S., Xilouris, E. M., Mavromatakis, F., Kapakos, E., Papamastorakis, J., & Goudis, C. D. 2006, MNRAS, 367, 1551
- Canto, J. 1981, "Investigating the Universe", ed. F. D. Kahn, (Dordrecht: Reidel), 95
- Cappellaro, E. Sabbadin, F., Benetti, S., Turatto, M. 2001, A&A, 377, 1035
- Carey, S.J.; et al. 2009, PASP, 121, 76
- Caswell, J.L. & Haynes, R.F. 1987, A&A, 171, 261
- Chiappini, C., Mateucci, F. & Meynet, G. 2003, A&A, 410, 257
- Chesneau, O., et al., 2007, A&A 473, L29
- Chu, Y.-H, et al. 2009, AJ, 138, 691
- Churchwell, E.B. et al. 2006, ApJ, 649, 759
- Churchwell, E.B. et al. 2009, 2009, PASP, 121, 213
- Ciardullo R., 2006, Proc. IAU Symp. 234, eds. Michael J. Barlow and Roberto H. Mndez. Cambridge: Cambridge University Press, pg. 325
- Ciardullo, R., 2010, PASA, 27, 149
- Ciardullo, R. et al. 2002, ApJ, 577, 31
- Cohen, M. 1993, AJ, 105, 1860
- Cohen, M. et al. 1989, ApJ, 341, 246
- Cohen, M. et al. 2007a, ApJ, 669, 343 (Paper-I)
- Cohen, M. et al. 2007b, MNRAS, 374, 979
- Cohen, M., Fitzgerald, M. P., Kunkel, W., Lasker, B., Osmer, P. C., 1978, ApJ, 221, 151
- Cohen, M., & Barlow, M.J. 1980, ApJ, 238, 58
- Cohen, M., & Green, A. 2001, MNRAS, 325, 531
- Cohen, M., et al. 2007b MNRAS, 374, 979
- Cohen, M., et al. 1989, ApJ, 341, 246
- Condon, J. J. & Kaplan, D. L., 1998, ApJS, 117, 361
- Condon, J.J., Cotton, W.D., Greisen, E.W., Yin, Q.F., Perley, R.A., Taylor, G. B. & Broderick, J.J. 1998, AJ, 115, 1693
- Corradi, R. L. M., Villaver, E., Mampaso, A., & Perinotto, M. 1997, A&A, 324, 276
- Corradi, R.L.M. et al. 2008, A&A, 480, 409
- Corradi, R.L.M., & Schwarz, H.E. 1995, A&A, 293, 871
- De Marco, O. 2009, PASP, 121, 316
- DePew, K., Parker, Q.A., Miszalski, B., De Marco, O., Frew, D.J., Acker, A. & Sharp, R. 2010, submitted to PASA
- Filipovic, M.D. et al. 2009, MNRAS, 399, 769
- Frew, D.J., Madsen, G.J., O'Toole, S.J., Parker, Q.A., 2010, PASA, 27, 203
- Frew D.J. & Parker Q.A., 2006, Proc. IAU Symp. 234, pg.395 eds. Michael J. Barlow and Roberto H. Mndez. Cambridge: Cambridge University Press,
- Frew D.J. & Parker Q.A., 2010, PASA, 27, 129
- Frew D.J. 2008, PhD Dissertation, Macquarie University, Australia
- Frew, D.J., Parker, Q.A. & Russeil, D., 2006, MNRAS, 372, 1081
- Green, A.J. 2002, Proc. IAU Symp. 199, eds. A. Pramesh Rao, G. Swarup, & Gopal-Krishna, pg.5259
- Greig, W. E., 1967, AJ, 72, 801
- Greig, W. E., 1971, A&A, 10, 161
- Gustafsson, B., Karlsson, T., Olsson, E., Edvardsson, B., & Ryde, N. 1999 A&A, 342, 426
- Hambly, N. C., Irwin, M. J., MacGillivray, H. T, 2001, MNRAS, 326, 1295
- Henize, K.G., 1954, PhD dissertation, University of Michigan
- Henize, K.G., 1967, ApJS, 14, 125
- Henry, R.B.C., Edmunds, M.G. & Köppen, J. 2000, ApJ, 541, 660
- Hewett, P.C. et al. 2003, ApJ, 599, 37
- Hora, J., L., & Latter, W. B. 1996, ApJ, 461, 288
- Hora, J., L., et al. 2008a, AJ, 135, 726
- Hora, J.L. et al. 2008b, PASP, 120, 1233

- Hora, J., L., Latter, W.B., Allen, L.E., Marengo, M., Deutsch, L.K., & Pipher, J.L. 2004, *ApJS*, 154, 296
- Hora, J., L., Latter, W. B., Deutsch, L.K., 1999, *ApJS*, 124, 195
- Jacoby, G.H. 1989, *ApJ*, 339, 39
- Jacoby, G.H., et al. 2010, *PASA*, 27, 156
- Kastner, J.H., Weintraub, D.A., Gatley, I., Merrill, K.M. & Probst, R.G. 1996, *ApJ*, 462, 777
- Kingsburgh R. L., & Barlow M. J., 1994, *MNRAS*, 271, 257
- Kohoutek, L. 2001, *A&A*, 378, 843
- Kuchar, T.A., Clark, F.O., 1997, *ApJ*, 488, 224
- Kwok, S. Zhang, Y., Koning, N.; Huang, H-H, Churchwell, E. B. 2008, *ApJS*, 174, 426
- Leisy, P., Dennefeld, M., Alard, C., Guibert, J. 1997, *A&AS*, 121, 407
- Lester, D. F. & Dinerstein, H.L 1984, *ApJ*, 281, L67
- Luo, S. G., Condon, J. J. & Yin, Q. F., 2005, *ApJS*, 159, 282
- Lutz, J. H., Kaler, J. B., Shaw, R. A., Schwarz, H. E., Aspin, C., 1989, *PASP*, 101, 966
- Madsen, G. J.; Reynolds, R. J.; Haffner, L. M. 2006, *ApJ*, 652, 401
- Manchado, A., Guerrero, M.A., Stanghellini, L., Serra-Ricart, M. 1996, “The IAC morphological catalog of northern Galactic planetary nebulae”
- Meaburn, J., & Walsh, J.R., 1989, *A&A*, 223, 277
- Miszalski, B., Acker, A., Moffat, A. F. J., Parker, Q. A., Udalski, A. 2009b, *A&A*, 488, 79
- Miszalski, B., Acker, A., Parker, Q. A., 2008a, *ASPC*, 391, 181
- Miszalski, B., Acker, A., Parker, Q. A., Moffat, A. F. J., 2009a, 505, 249
- Miszalski, B., Parker, Q. A., Acker, A., Birkby, J. L., & Frew, D. J., Kovacevic, A. 2008b, *MNRAS*, 384, 525
- Mizuno, D.R., Kraemer, K. E., Flagey, N., Billot, N., Shenoy, S., Paladini, R., Ryan, E., Noriega-Crespo, A., & Carey, S. J., 2010, *AJ*, 139, 1552
- Moe, M. & De Marco, O. 2006a, *Proc. IAU. Symp.* 234, p.463, eds. Michael J. Barlow and Roberto H. Mendez. Cambridge: Cambridge University Press, p.463
- Moe, M. & De Marco, O. 2006b, *ApJ*, .650, 916
- Morgan, D.H., Parker, Q.A., & Cohen, M. 2003, *MNRAS*, 346, 719
- Murphy, T., Cohen, M., Ekers, R., Green, A., Wark, R., Moss, V. *MNRAS*, 405, 1560
- Murphy, T., Mauch, T., Green A., Hunstead R. W., Pietrzynska, B.; Kels, A. P., Sztajer, P. 2007, *MNRAS*, 382, 382
- Parker, Q.A. et al. 2005, *MNRAS*, 362, 689
- Parker, Q.A. et al. 2006, *MNRAS*, 373, 79
- Pazderska et al. 2009, *A&A* 498, 463
- Peeters, E. et al. 2002, *A&A*, 381, 571
- Peimbert M., & Serrano A., 1980, *RMx&A*, 5, 9
- Peimbert M., & Torres-Peimbert S., 1983, in Flower D. R., ed, *IAU Symp.* Vol. 103, Planetary Nebulae. Dordrecht, Reidel, p.233
- Peimbert M., 1978, in Terzian, Y., ed., *IAU Symp.* Vol. 76, Planetary Nebulae: Observations and Theory (D. Reidel, Dordrecht), p.215
- Phillips, J., P., 2008, *MNRAS*, 361, 283
- Phillips, J.P. & Ramos-Larios, G. 2005, *MNRAS*, 364, 863
- Phillips, J., P., & Ramos-Larios, G., 2008, *MNRAS*, 386, 995
- Phillips, J.P. & Ramos-Larios, G. 2009, *MNRAS*, 396, 1915
- Phillips, J., P. & Zepeda-Garcia, D., 2009, *MNRAS*, 394, 1875
- Ramos-Larios, G. & Phillips, J. P. 2008, *MNRAS*, 390, 1014
- Ramos-Larios, G., Guerrero, M., Suárez, O., Miranda, L.F., & Gómez, J. F. 2009, arXiv:0903.1131v1
- Reach, W.T. et al. 2005, *PASP*, 117, 978
- Reid, W.A., & Parker, Q.A. 2006, *MNRAS*, 373, 521
- Reid, W.A., & Parker, Q.A. 2010, *PASA*, 27, 187
- Richer, M.G. et al. , 2008, *ApJ*, 689, 203
- Riesgo, H. & Lopez, J.A. 2006. *RMxAA*, 42, 47
- Robitaille, T.P., Whitney, B.A., Indebetouw, R., Wood, K., & Denzmore, P. 2006, *ApJS*, 167, 256
- Ruffle, P.M.E., Zijlstra, A.A., Walsh, J.R., Gray, M.D., Gesicki, K., Minniti, D., & Comeron, F. 2004, *MNRAS*, 353, 796
- Sabbadin, F., Minello, S., & Bianchini, A. 1977, *A&A*, 60, 147 (SMB)
- Santander-Garcia, M., et al. , 2008, *A&A*, 485, 117
- Schmeja, S. & Kimeswenger, S. 2001, *A&A*, 377, 18
- Sewilo et al. 2009, “The SAGE Data Products Description”, <http://ssc.spitzer.caltech.edu/spitzermission/observingprograms/legacy/sage/>
- Shaw, R.A., Kaler, J.B., 1989, *ApJS*, 69, 495
- Shaw, R.A., Rest, A., Damke, G. 2009, *The Magellanic System: Stars, Gas, and Galaxies*, eds. Jacco Th. van Loon and Joana M. Oliveira, *IAU Symp.* 256 (CUP)
- Shaw, R.A., Rest, A., Damke, G., Smith, C., Read, W.A., & Parker, Q.A. 2007, *ApJ*, 669, 25
- Smith, N. & Gehrz, R.D., 2005, *AJ*, 129, 969
- Smith, N. 2003, *MNRAS*, 342, 383
- Soker, N. 2004, *ASPC*, 313, 562
- Stanghellini, L. 2000, *ApSS*, 272, 181
- Stanghellini, L., et al. 2007, *ApJ*, 671, 1669
- Suárez, O., Garca-Lario, P., Manchado, A., Manteiga, M., Ulla, A., Potasch, S. R., 2006 *A&A*, 458, 173
- Tajitsu, Akit, Tamura, S., Yadoumaru, Y., Weinberger, R. & Köppen, J. 1999, *PASP*, 111, 1157
- Todt, H., Pea, M., Hamann, W.-R., & Grfener, G. 2010, arXiv:1003.3419v1

- Treffers, R. R., Fink, U., Larson, H. P., & Gautier, T. N., III, 1976, *ApJ*, 209, 793
- Tylenda, R., 1989, in Torres-Peimbert S., ed, *IAU Symp. Vol. 131, Planetary Nebulae* (Kluwer; Dordrecht), p.175
- Tylenda, R., Sidmiak, N., Grny, S. K., Corradi, R. L. M., & Schwarz, H. E. 2003, *A&A*, 405, 627
- Van der veen, W., E., C., J., Habing, H., J., & Geballe, T., R., 1989, *A&A* 226,108
- Wachter, S., Mauerhan, J. C., Van Dyk, Schuyler D., Hoard, D. W., Kafka, S., & Morris, P. W. 2010, *AJ*, 139, 2330
- Wainscoat, R., Cohen, M., Volk, K., Walker, H.J., & Schwartz, D.E. 1992, *ApJS*, 83, 111
- Webster, B.L., et al. 1978, *MNRAS*, 185, 45
- Westerlund, B.E. & Henize, K.G., 1967, *ApJS*, 14,154
- Whitelock, P.A., 1985, *MNRAS*, 213, 59
- Whitney, B.A. et al. , 2008, *AJ*, 136, 18
- Ybarra, J.,E., & Lada, A., E. 2009, *ApJ*, 695, L120
- Zhang, H. & Kwok, S. 2009, *ApJ*, 706, 252
- Zuckerman, B., & Gatley, I., 1988, *ApJ*, 324, 501

APPENDIX A: OBJECTS REMOVED FROM OUR ORIGINAL SAMPLE

Based on our careful re-evaluation of the provenance of our combined sample, especially important for the previously known pre-MASH PNe, we have been able to eliminate 25 objects from our compilation. Some PNe were not observed at all by GLIMPSE due to the jagged boundaries in Galactic coordinates. Nebulae without any IRAC observations are: PHR1654-4143, and MPA1525-5528.

See Table A1 for objects which we reject from our original sample of PN candidates. Note that no MASH-II objects were rejected as non-PNe in our surveyed area and only 5 MASH-I PNe (which tend to be more extended than MASH-II) were removed while 20 “known” PNe have been eliminated. We suggest the most probable classification for each of these and document the reasons for such rejections. Most are HII regions and can be recognized as such from their MIR morphology, false colours, high brightness, apparent size, large radio flux densities, and their characterization in the literature as bubbles. In the notes on the right of the table the abbreviations C06, K08, and P06 denote Churchwell et al. (2006), Kwok et al. 2008, and Parker et al. (2006). The first two papers focus on bubbles, i.e., HII regions (C06); IRAC images of nebulae (K08). Note that P06 reject non-PNe typically because of morphology and optical spectroscopy although other criteria such as 2MASS colours and MSX detections were also employed.

Table A1. Objects rejected as non-PNe.

Name	RAJ2000	DecJ2000	GLON deg	GLAT status	MASH deg	Nature	Reason rejected/by whom
G295.7-00.2	11 49 11.8	−62 12 29	295.747	−00.208	-	HII region	MSX source; P06 morphology; K08, Fig.5
G296.31+00.68	11 55 37.92	−61 28 16.7	296.319	0.68	-	emission line star	PM 1-61
G298.18-00.78	12 09 01.2	−63 15 58	298.183	−0.786	-	compact HII region	He 2-77: this paper
G298.4+00.6	12 13 09.0	−61 50 28	298.431	+0.696	-	HII region	this: morphology; very large radio flux; (K08, Fig.6
G301.2+00.4	12 37 09.6	−62 23 10	301.278	+0.440	-	HII region	this paper: morphology; K08, Fig.7 incorrectly 301.1+00.4)
PHR1253-6350	12 53 7.3	−63 50 32	303.118	−0.969	P	Symbiotic star	Spectrum (Paper-I)
G306.4+ 00.2	13 21 36.2	−62 29 47	306.407	+00.172	-	ISM	due to diffuse ISM (this paper) K08, Fig.8
G321.0-00.7	13 22 05.5	−62 24 06	306.474	+00.259	-	Reflection nebula?	Fuzz around CPD-61 3629: K08, Fig.10
PHR1346-6116	13 46 38.2	−61 16 27	309.516	0.891	L	ISM	This paper; see Fig. 2
G309.80+00.56	13 49 32.64	−61 31 43.3	309.8	0.566	-	Pop-I WR nebula; WR 59, Simbad	
G309.5-00.7	13 49 52.1	−62 49 41	309.546	−0.709	-	HII region	C06; very large radio flux; K08, Fig.9
PHR1356-6139	13 56 44.8	- −61 39 44	310.598	0.234	P	ISM	due to diffuse ISM (this paper)
G321.3-00.3	15 17 31.2	−57 51 10	321.392	−0.311	-	HII region	PHR1517-5751 rejected in Paper-I; very large radio flux; C06; K08, Fig.11
G321.20-00.82	15 18 21.84	−58 23 12.5	321.204	−0.827	-	Post-AGB Star	PN PM 1-88: orange 2mass, MIR white; this paper;
G328.5-00.5	15 59 38.2	−53 45 32	328.573	−00.531	-	HII region	RCW99 P06 morphology; very large radio flux; K08, Fig.12
PHR1603-5402	16 03 41.4	−54 02 04	328.841	−1.131	L	MSX 1arcmin source	
G329.6-00.4	16 04 53	−53 00.7	329.654	−00.484	-	HII region	S69: rejected by P6 & this paper; morphology; very large radio flux; C06; K08, Fig.12
G332.5-00.1	16 16 56.40	−50 47 22.6	332.528	−00.121	-	HII region	PHR J1616-5047; P06 morphology; very large radio flux; K08, Fig.13
G331.72-01.01	16 17 13.39	−51 59 10.3	331.727	−01.011	-	Symbiotic star/B[e]	Mz 3: this paper
G333.7+00.3	16 20 09.4	−49 36 09	333.726	+0.368	-	HII region	PHR J1620-4936 rejected (this paper) for morphology; very large radio flux; K08, Fig.13
G340.0+00.9	16 43 16.00	−44 35 18.0	340.071	+0.927	-	HII region	YSO? PHR J1643-4435; this paper; morphology; K08, Fig.14
PHR1644-4455	16 44 36.2	−44 55 23	339.973	0.528	P	diffuse ISM	(this paper)
G018.6-00.0	18 25 10.46	−12 42 15.6	18.656	−0.058	-	HII region	P06 for morphology; very large radio flux; K08, Fig.2
G026.47+00.02	18 39 32.16	−05 44 19.6	26.470	0.021	-	HII region	emission line MSX source; LBV candidate
G055.5-00.5	19 36 11.0	19 43 29	55.492	−0.495	-	IRAS source	not a PN in SIMBAD